Molecular Crystals and Liquid Crystals Science and Technology. Section A. Molecular Crystals and Liquid Crystals

Publication details, including instructions for authors and subscription information:
http://www.tandfonline.com/loi/gmcl19

Transient Periodic Dissipative Structures in Nematics Confined between Coaxial Cylinders

U. D. Kini [a]

[a] Raman Research Institute, Bangalore, 560 080, INDIA

Version of record first published: 24 Sep 2006

To cite this article: U. D. Kini (1999): Transient Periodic Dissipative Structures in Nematics Confined between Coaxial Cylinders, Molecular Crystals and Liquid Crystals Science and Technology. Section A. Molecular Crystals and Liquid Crystals, 333:1, 79-122

To link to this article: http://dx.doi.org/10.1080/10587259908025998

Mol. Cryst. Liq. Cryst., Vol. 333, pp. 79-122
Reprints available directly from the publisher
Photocopying permitted by license only

Transient Periodic Dissipative Structures in Nematics Confined between Coaxial Cylinders

U.D. KINI*

Raman Research Institute, Bangalore – 560 080, INDIA

(Received 01 May, 1998; In final form 30 December, 1998)

The onset of transient periodic dissipative structures (*TPDS*) is studied using the linear perturbation approximation when a sufficiently strong magnetic field (**B**) is impressed on the uniformly aligned director ($\mathbf{n_0}$) of a nematic confined to the annular space between two coaxial cylinders of radii R_2 and R_1 ($R_2 > R_1$). Only *TPDS* with axial or azimuthal periodicity is considered. An approximate expression for the magnetic body force density is employed. The solutions mainly concern rigid anchoring. When $\mathbf{n_0}$ is along the common axis, a radial field or an azimuthal field causes *TPDS* with periodicity along the axis when the calamitic nematic has positive diamagnetic anisotropy ($\chi_A > 0$); an axial field has a similar effect when $\chi_A < 0$. The dependence of the rise time as well as the periodicity wavevector are studied as functions of the applied field strength and the ratio of the radii ($R_{21} = R_2/R_1$). A weakening of director anchoring has a deleterious effect on the formation of *TPDS*. When $\mathbf{n_0}$ is azimuthal and $\chi_A > 0$, a radial or an axial field may induce *TPDS* having an azimuthal periodicity wavevector which is an integer and related to the number of domains; continuous changes in control variables cause discontinuous changes in the wavevector. Using hypothetical material parameters, it is shown that an axial (or an azimuthal) field may induce *TPDS* with a continuously varying (or discontinuously varying) wavevector in a radially aligned discotic nematic having $\chi_A > 0$. If $\chi_A < 0$, a radial field may induce *TPDS* with modulation along both the axial and the azimuthal directions in a discotic nematic. When R_{21} is close to unity, the results of this work go over to those obtained for a flat sample.

Keywords: Anchoring energy; Freedericksz transition; Instabilities; Maxwell stress; Periodic deformations; Scaling laws; Transient phenomena

1. INTRODUCTION

The anisotropic physical properties of nematics manifest themselves through a variety of static and dynamic effects under the action of electric (**E**) and **B** fields. Most of these phenomena have been satisfactorily explained by the continuum

* Correspondence Author: email address: udkini@rri.ernet.in

theory [1–4]. The application of a gradually strengthening **B** normal to $\mathbf{n}_0$ in a nematic with positive χ_A causes a static non-periodic deformation (*NPD*) [5] or a periodic distortion (*PD*) [6] above a well defined threshold, depending upon the elastic anisotropy, surface treatment [7], etc. When the applied **B** is removed, the director field relaxation is generally accompanied by aperiodic back-flow [8]. On the other hand, the sudden application of a strong **B** normal to $\mathbf{n}_0$ leads to *TPDS* in various types of nematics confined to different configurations [9]. In this case, convective structures form inside the nematic sample immediately after the application of the strong **B**; these dissipative structures exist for some time and then disappear, leaving the sample in a final equilibrium state. Though the phenomenon is basically non-linear, a simplified linear approach has been suggested by Guyon *et al* [10] for rigid director anchoring; this solution technique enables the computation of the periodicity wavevector (*PWV*) as well as the rise time at the instant of field application. The results of these calculations compare favourably with the experimental observations [9]. Attempts have been made [9] to study the influence of geometry and different parameters on the formation of *TPDS*. The effect of weak director anchoring has been worked out for the twist geometry [11]. The literature quoted in [6–11] concerns flat nematic samples that are limited by plane parallel plates. As the cells are generally thin, the samples can be assumed to be confined only along one spatial direction (viz., the direction normal to the plates). The applied **B** is also assumed to be constant in theoretical calculations.

It is possible to study nematic samples that are confined between coaxial cylinders. Even for long cylinders, such a sample will be limited along two mutually orthogonal curvilinear coordinates (the radial and the azimuthal) and this is bound to lead to new forms of behaviour when R_{21} is significantly different from unity. Suppose $\mathbf{n}_0$ is aligned parallel to the cylinder walls. The response to an applied **B** may be different depending upon whether $\mathbf{n}_0$ lies along the axis or perpendicular to it. Treating the surfaces of cylinders to produce a specific director anchoring is a difficult task; it is also not easy to make optical observations on cylindrical samples. Hence, not many experimental studies have been reported on the cylindrical geometry. Flow induced periodic instabilities have been studied experimentally [12] and interpreted theoretically [12, 13]. Thermal convective instabilities have been observed in nematics confined between rotating coaxial cylinders that are maintained at different temperatures [14]. Some theoretical studies have also been reported on static distortions. Using the rigid anchoring hypothesis, it is shown [15] that the *NPD* magnetic threshold is strongly dependent on R_{21} and that for certain $\mathbf{n}_0$, the *NPD* threshold vanishes when R_{21} takes sufficiently high values; this can be interpreted as a *geometric threshold*. These ideas have been extended to *PD* [16] in nematics that possess

high elastic anisotropy. Depending upon $\mathbf{n}_0$, it is shown [16] that the geometric threshold may exist for *PD* and that the variation of *PWV* with different parameters may occur continuously or in discrete steps. The influence of weak director anchoring on the *NPD* threshold as well as the growth rates of aperiodic reorientation in various configurations forms the subject of [17].

Recently, efforts have been made to impart uniform director alignment even for curved surfaces [18]. It now appears that convenient experimental checks on theoretical predictions in the cylindrical geometry may become feasible. It should be interesting to carry forward the ideas of [15–17] into a theoretical analysis of *TPDS* in the cylindrical geometry for different configurations. It is well known [15–17] that **B** that conforms to cylindrical symmetry becomes a function of the coordinates. Such a field not only produces a torque on the director field, but also contributes a body force density (the spatial divergence of the Maxwell stress [19]) that can influence the occurrence of transient flow in a fluid medium.

This provides the motivation for the present work. The different symmetric configurations are listed in section 2. Section 3 contains results for *TPDS* in an axially oriented nematic for both rigid and weak anchoring. Section 4 considers the case of azimuthal director orientation. Both sections 3 and 4 concern a typical calamitic nematic. Hypothetical material parameters are chosen to represent a discotic nematic (section 5) for which only the radial orientation is considered. Section 6 summarizes the main conclusions.

2. CONFIGURATIONS

The length of each cylinder is assumed to be large compared to $R_2 - R_1$, the difference in the radii. The cylindrical coordinate system is chosen with r, ψ, z being the radial, the azimuthal and the axial coordinates. Physical components of tensors are employed throughout. The fluid is assumed to be incompressible, Three symmetric $\mathbf{n}_0$ are possible. These are the *axial alignment,*

$$\mathbf{n}_o = (0,\ 0,\ 1)\,, \tag{1}$$

the *azimuthal alignment,*

$$\mathbf{n}_o = (0,\ 1,\ 0)\,, \tag{2}$$

and the *radial alignment,*

$$\mathbf{n}_o = (1,\ 0,\ 0)\,. \tag{3}$$

In conformity with Maxwell's equations [19] and cylindrical symmetry, a general form of the magnetic intensity may be taken to be

$$\mathbf{H} = \left(\frac{X}{r}, \frac{Y}{r}, H_z\right)$$

where H_z, X and Y are constants. In its symmetric form, **H** can be [20] either *axial,*

$$\mathbf{H} = (0, 0, H_z)\,;\; X = 0 = Y \tag{4}$$

or *azimuthal,*

$$\mathbf{H} = \left(0, \frac{Y}{r}, 0\right)\,;\; X = 0 = H_z \tag{5}$$

or *radial,*

$$\mathbf{H} = \left(\frac{X}{r}, 0, 0\right)\,;\; Y = 0 = H_z. \tag{6}$$

A suitable combination of two of the above fields can lead to the analogue of the *oblique field* studied with flat samples [5].

In real nematic samples, the director field does not stay strictly along $\mathbf{n_0}$ due to fluctuations. When a strong **H** is applied along a suitable direction, it exerts a reorienting torque causing the director field to change in time. The time varying director field creates a viscous stress which produces flow in the sample. The velocity gradients associated with the flow cause a viscous torque on the director field completing the coupling between the flow and the orientation. Immediately after **H** is impressed, the director and velocity perturbations can be assumed to be small. This is the basis for the derivation of the governing equations. We first study the axial alignment.

3. AXIAL INITIAL ORIENTATION

$\mathbf{n_0}$ is given by (1). In equilibrium in the absence of **H,** the hydrostatic pressure is constant throughout the sample at some (indeterminate) value, p_o, say. Immediately after impressing **H,** the director and velocity fields are given by

$$\mathbf{n} = \left(\theta, \phi, 1 - \frac{\theta^2 + \phi^2}{2}\right), \tag{7}$$

$$\mathbf{V} = (v_r, rw, v_z), \tag{8}$$

where $\theta, \phi, v_r, \omega$ and v_z are assumed to be linear perturbations and are associated with the pressure perturbation, p; all perturbations are functions of r, ψ, z and t;

we note that ω is an angular velocity. Two torque equations result corresponding to the two director perturbations. In the torque balance, the moment of inertia density of the director field is ignored. Three force equations describe the three components of the acceleration of the fluid, but of these only two are independent as the pressure perturbation, p, gets eliminated. However, they are supplemented by the equation of continuity,

$$\frac{\partial v_r}{\partial r} + \frac{\partial w}{\partial \psi} + \frac{v_r}{r} + \frac{\partial v_z}{\partial z} = 0. \tag{9}$$

The rest of the governing equations are

$$K_1\frac{\partial^2\theta}{\partial r^2} + \frac{K_1}{r}\frac{\partial\theta}{\partial r} + \frac{K_2}{r^2}\frac{\partial^2\theta}{\partial\psi^2} + K_3\frac{\partial^2\theta}{\partial z^2} + \frac{(m_1 - K_1)}{r^2}\theta + m_3\theta - \gamma_1\frac{\partial\theta}{\partial t} - \frac{(K_1 + K_2)}{r^2}\frac{\partial\phi}{\partial\psi} + \frac{(K_1 - K_2)}{r}\frac{\partial^2\phi}{\partial r\partial\psi} + \frac{m_2}{r^2}\phi - \mu_3\frac{\partial v_z}{\partial r} - \mu_2\frac{\partial v_r}{\partial z} = 0 \tag{10}$$

$$K_2\frac{\partial^2\phi}{\partial r^2} + \frac{K_2}{r}\frac{\partial\phi}{\partial r} + \frac{K_1}{r^2}\frac{\partial^2\phi}{\partial\psi^2} + K_3\frac{\partial^2\phi}{\partial z^2} + \frac{(m_4 - K_2)}{r^2}\phi + m_3\phi - \gamma_1\frac{\partial\phi}{\partial t} + \frac{(K_1 + K_2)}{r^2}\frac{\partial\theta}{\partial\psi} + \frac{(K_1 - K_2)}{r}\frac{\partial^2\theta}{\partial r\partial\psi} + \frac{m_2}{r^2}\theta - \frac{\mu_3}{r}\frac{\partial v_z}{\partial\psi} - \mu_2 r\frac{\partial\omega}{\partial z} = 0 \tag{11}$$

$$2\eta_A\frac{\partial^2 v_r}{\partial r^2} + \frac{\eta_A}{r^2}\frac{\partial^2 v_r}{\partial\psi^2} + \frac{2\eta_A}{r}\frac{\partial v_r}{\partial r} - \frac{2\eta_A}{r^2}v_r + \eta_C\frac{\partial^2 v_r}{\partial z^2} + \eta_A\frac{\partial^2\omega}{\partial r\partial\psi} - \frac{2\eta_A}{r}\frac{\partial\omega}{\partial\psi} + \eta_D\frac{\partial^2 v_z}{\partial r\partial z} + \mu_2\frac{\partial^2\theta}{\partial z\partial t} = \frac{\partial p}{\partial r} + \rho\frac{\partial v_r}{\partial t} \tag{12}$$

$$\frac{\eta_A}{r}\frac{\partial^2 v_r}{\partial r\partial\psi} + \frac{3\eta_A}{r^2}\frac{\partial v_r}{\partial\psi} + \eta_A r\frac{\partial^2\omega}{\partial r^2} + \frac{2\eta_A}{r}\frac{\partial^2\omega}{\partial\psi^2} + \eta_C r\frac{\partial^2\omega}{\partial z^2} + 3\eta_A\frac{\partial\omega}{\partial r} + \frac{\eta_D}{r}\frac{\partial^2 v_z}{\partial\psi\partial z} + \mu_2\frac{\partial^2\phi}{\partial z\partial t} = \frac{1}{r}\frac{\partial p}{\partial\psi} + \rho r\frac{\partial\omega}{\partial t} \tag{13}$$

$$\eta_D \frac{\partial^2 v_r}{\partial r \partial z} + \frac{\eta_D}{r}\frac{\partial v_r}{\partial z} + \eta_D \frac{\partial^2 \omega}{\partial \psi \partial z} +$$
$$\eta_B \frac{\partial^2 v_z}{\partial r^2} + \frac{\eta_B}{r^2}\frac{\partial^2 v_z}{\partial \psi^2} + \frac{\eta_B}{r}\frac{\partial v_z}{\partial r} + 2\nu_1 \frac{\partial^2 v_z}{\partial z^2} +$$
$$\mu_3 \frac{\partial^2 \theta}{\partial r \partial t} + \frac{\mu_3}{r}\frac{\partial \theta}{\partial t} + \frac{\mu_3}{r}\frac{\partial^2 \phi}{\partial \psi \partial t} = \frac{\partial p}{\partial z} + \rho \frac{\partial v_z}{\partial t} \qquad (14)$$

$$m_1 = \chi_A X^2;\ m_2 = \chi_A XY;\ m_3 = -\chi_A H_z^2;\ m_4 = \chi_A Y^2; \qquad (15)$$

where γ_1 is the rotational viscosity, η_A, η_B, η_C the Miesowicz viscosities [21] and ν_1 the extensional viscosity of the nematic [22]; $\eta_D = (\eta_B + \eta_C - \gamma_1)/2$; K_1, K_2, K_3 are the splay, twist and bend curvature elastic constants, respectively; μ_2 and μ_3 are torque viscosity coefficients [21]; ρ is the density. It is customary [8, 10] to ignore the inertial terms containing ρ as the contribution of these terms is negligible for sufficiently thin samples. As most of the calculations are performed numerically, the inertial terms have been retained as they do not increase the complexity of computations. With respect to r variation, θ and ϕ are, respectively, splay and twist deformations. In the force equations (12) – (14), the components of the body force arising out of the spatial variation of **H** are absent (Appendix 1). Depending upon the choice of **H**, only some of the m_i of (15) will be non-zero.

The governing equations (9) -(14) have to be supplemented by the boundary conditions. For the velocities, the no-slip condition at the boundaries is assumed so that

$$v_r = 0,\ w = 0,\ v_z = 0 \text{ at } r = R_1 \text{ and } r = R_2 \text{ for all times } t. \qquad (16)$$

If the director anchoring at the two substrates is not rigid, the Rapini – Papoular form of surface free energy density (W_s) can be adopted [7]. In general, the anchoring strengths for θ and ϕ are different. It may also be possible to impart different surface treatment to the two substrates. Hence,

$$W_S = \frac{A_{\theta 1}}{2}\theta^2 + \frac{A_{\phi 1}}{2}\phi^2 \text{ at } r = R_1$$
$$W_S = \frac{A_{\theta 2}}{2}\theta^2 + \frac{A_{\phi 2}}{2}\phi^2 \text{ at } r = R_2 \qquad (17)$$

where the A_θ and A_ϕ are, respectively, the splay and twist anchoring strengths. By minimizing the total free energy of the sample, the following boundary conditions result and are valid for all t:

$$\tau_\theta - A_{\theta 1}\theta = 0 \text{ at } r = R_1\ ;\ \tau_\theta + A_{\theta 2}\theta = 0 \text{ at } r = R_2\ ;$$
$$\tau_\phi - A_{\phi 1}\phi = 0 \text{ at } r = R_1\ ;\ \tau_\phi + A_{\phi 2}\phi = 0 \text{ at } r = R_2\ ; \qquad (18)$$

$$\tau_\theta = K_1 \frac{\partial \theta}{\partial r} + \frac{(K_1 - K_{24})}{r}\left(\theta + \frac{\partial \phi}{\partial \psi}\right);$$
$$\tau_\phi = K_2 \frac{\partial \phi}{\partial r} + \frac{(K_2 - K_{24})}{r}\left(\phi - \frac{\partial \theta}{\partial \psi}\right),$$

where K_{24} is the *saddle-splay* surface elastic constant which is of the same magnitude as the bulk elastic constants [23]. For understanding scaling arguments, it is convenient to define r in terms of the dimensionless variable ξ such that

$$r = h(\xi + a);\ h = \frac{(R_2 - R_1)}{2};\ a = \frac{(R_2 + R_1)}{(R_2 - R_1)}. \tag{19}$$

The range $R_1 \leq r \leq R_2$ gets mapped into $-1 \leq \xi \leq 1$. When the anchoring is sufficiently strong and the sample not too thin, the dimensionless quantity $h\,A/K \gg 1$ where A is an anchoring strength and K a curvature elastic constant. In this limit, (18) can be simplified by assuming the rigid anchoring hypothesis which requires that the director perturbations vanish at the boundaries at all t:

$$\theta = 0\ ;\ \phi = 0\ at\ r = R_1,\ r = R_2. \tag{20}$$

We adopt (16) and (20) in this work except in section 3.2. Solutions for different situations are obtained by taking the relevant subsets of terms from the governing equations (9) – (14) and solving them with the appropriate boundary conditions. To solve for the static case, for instance, time dependence is dropped and the velocity field assumed to vanish. The torque equations (10) and (11) are considered. If the *NPD* threshold is required. θ and ø are assumed to depend only on r. To study aperiodic dynamic reorientation (*AR*), all perturbations are assumed to depend on r and t; then the appropriate subset of equations (9) – (14) is chosen depending upon whether flow couples to orientation or not.

3.1 Azimuthal Field; Rigid Anchoring; $\chi_A > 0$

The first task is to fix a reference field and this is generally the *NPD* threshold. Assuming dependence on only r and ignoring **V**, we find that θ gets decoupled from ø and also damps out as it is unaffected by **H**. The solution of (11) and (20) reduces to that of an eigenvalue problem. The condition for the existence of ø yields the *NPD* threshold Y_F given by

$$Y_F^2 = \left(\left(\frac{\pi}{\ln(R_{21})}\right)^2 + 1\right)\frac{K_2}{\chi_A}, \tag{21}$$

so that for $Y > Y_F$, the twist distortion, ø, develops in the sample; but the amplitude of ø becomes indeterminate. Clearly, ø is asymmetric with respect to

$r = (R_1 + R_2)/2$ and its extremum occurs at the geometric mean radius $r_G = \sqrt{R_1 R_2}$. A geometrical threshold cannot exist; ie., (21) does not yield a real solution for R_{21} if we equate Y_F to zero. We can now define a reduced field

$$R_Y = \frac{Y}{Y_F} \tag{22}$$

to measure the strength of **H**. One advantage of stating results in terms of R_Y is that the actual value of χ_A need not be known.

For *AR*, the splay distortion θ couples with the back-flow v_z [8] but ϕ remains uncoupled to the remaining perturbations. The $\theta - v_z$ mode damps out as it has no driving term. The ϕ mode (**MODE N1**) exists as before except that now the time variation of the twist ϕ is damped due to the presence of the twist viscosity γ_1. The governing equation (11) permits a separation of variables of the form

$$\phi = P(r) \exp(st)$$

where s the growth rate. Substitution in (11) results in an ordinary differential equation (*ODE*) in $P(r)$. At a given value of R_Y, (11) and (20) can be solved numerically to determine s_A. Appendix 2 briefly outlines the numerical technique employed in this work. The material parameters for a typical calamitic nematic (*5CB* at 28° C) are used [26]:

$$(K_1, K_2, K_3) = (5.21, 2.71, 6.67)\, 10^{-7} \text{ dyne};$$
$$(\eta_A, \eta_B, \eta_C, \gamma_1, \nu_1) = (0.358, 0.161, 0.973, 0.728, 0.412) \text{ poise}. \tag{23}$$

For purpose of calculation, the values $\chi_A = 1.0\ 10^{-7}$ emu and $\rho = 1$ gm cm^{-3} are fixed. By substituting for the different parameters, s_A can be calculated numerically. For $R_Y \leq 1$, $s_A \leq 0$; $s_A > 0$ when $R_Y > 1$. Thus, *MODE N1* grows with time when the impressed **H** is stronger than the threshold (21). As the perturbations are assumed to be linear, we understand that $s_A$represents the *instantaneous growth rate of MODE N1* at the time of applying **H**.

Previous studies on the twist geometry in flat samples indicate [27] that when a sufficiently strong **H** is impressed in the plane of the sample normal to the initial planar $\mathbf{n_0}$, *TPDS* is observed with periodicity along $\mathbf{n_0}$; *TPDS* in this case is associated with a twist deformation that couples with a flow that occurs in the sample plane but normal to $\mathbf{n_0}$. The theoretical interpretation for the occurrence of *TPDS* is the following. *AR* is associated with the effective viscosity, γ_1. If *PWV*of *TPDS* is high enough, the effective viscosity of *TPDS* becomes substantially less than γ_1. Analogously with the results of [27], one can expect *TPDS* in the present case with periodicity along z.

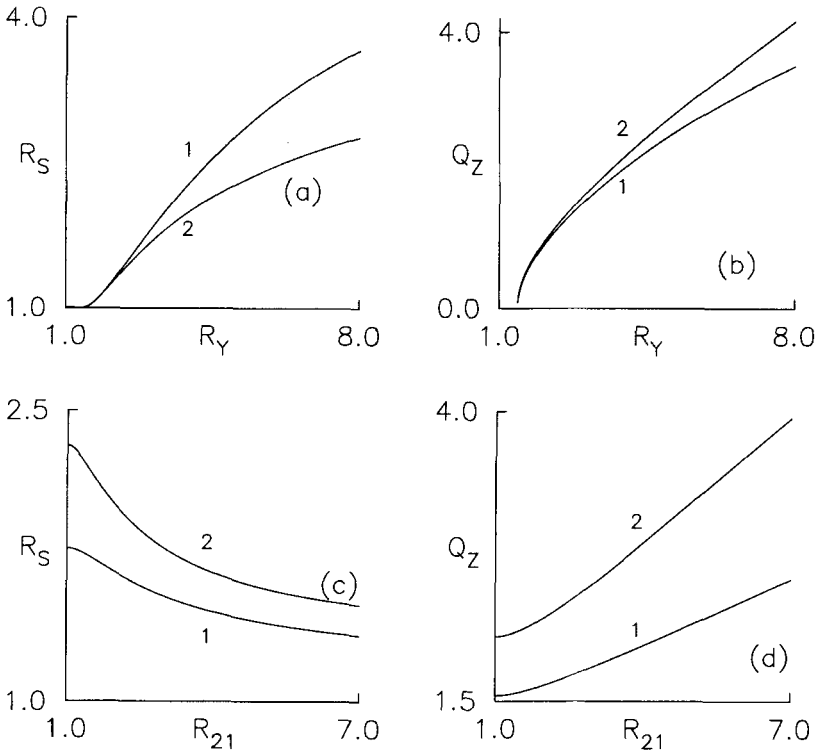

FIGURE 1 Axially aligned nematic (1) with material parameters (23) subjected to the action of azimuthal **H** (5). R_{21} is the ratio of the radii of two coaxial cylinders. *MODE P*1 is the fastest growing periodic perturbation with periodicity along z (the cylinder length), instantaneous growth rate s_P and dimensionless wavevector Q_Z. *MODE N*1 is the aperiodic mode with growth rate s_A. $R_S = s_P/s_A$ is the dimensionless growth rate. The dimensionless field strength $R_Y = Y/Y_F$ where the threshold Y_F is given in (21). Figures 1a, 1b: plots of R_S and Q_Z versus R_Y at R_{21} = (1) 1.02 (2) 2. Figures 1c, 1d: plots of R_S and Q_Z as functions of R_{21} for R_Y = (1) 3 (2) 4. (see section 3.1). The effect of an axial **H** on a material with negative χ_A is similar except for some important differences (see section 3.3 and Figure 4)

With the assumption that all perturbations depend on r, z and t, the perturbations get divided into two uncoupled sets. The set involving θ, v_r and v_z damps out as θ is not associated with a driving magnetic torque. The other set (**MODE P1**) contains ϕ and ω which are controlled by (11), (13). The variables z and t can be separated by the substitution

$$(\phi, w) = (P(r)\cos(qz), \Omega(r)\sin(qz))\ \exp(st)$$

where **q** is *PWV* along z. Clearly, ϕ and ω are out of phase along z. Substitution in (11) and (13) results in two coupled, *ODE*s which can be solved numerically to obtain the growth rate of *MODE P*1, s_P, the dimensionless wavevector, Q_Z, and

the reduced growth rate, R_S. If $R_S > 1$, *MODE P*1 grows faster than *MODE N*1 and we say that *TPDS* can set in; in this case, transient (circular) stripes should appear normal to the axis of the cylinders. If $R_S < 1$, *AR* occurs and stripes cannot appear. If we regard Q_Z as the order parameter separating the two kinds of transient phenomena, the condition $R_S = 1$ will define a critical point provided that Q_Z vanishes in the same limit. Comparison of the governing equations for *MODE P*1 and *MODE N*1 (see Appendix 2) shows that a critical point will exist if $\Omega \to 0$ when $Q_Z \to 0$. It is found that this indeed happens.

Figure 1 depicts the variations of R_S and Q_Z with R_Y and R_{21}. When R_Y is high enough, *MODE P*1 grows faster than *MODE N*1 (Figures 1a, 1b). For a given R_{21}, R_S and Q_Z decrease with decreasing R_Y; when R_Y approaches a lower limit, R_{YC}, R_S approaches unity while Q_Z vanishes showing that *AR* exists for $1 < R_Y < R_{YC}$. Using Q_Z as an order parameter of the striped phase, we can regard R_{YC} as a critical point. The value of R_{YC} does not depend strongly on R_{21}. At a given R_Y, Q_Z increases with R_{21} but R_S diminishes (the growth rate of *MODE P*1 becomes closer to that of *MODE N*1). If h is fixed and R_{21} augmented, one can say that the increase in Q_Z should represent a narrowing of the stripes associated with *TPDS*. Figures 1c, 1d which show the variations with R_{21} at fixed R_Y reflect these results. Clearly, the critical field, R_{YC}, must vary with R_{21} for a given material. It is not possible to obtain an analytical expression for R_{YC}; hence, R_{YC} is determined numerically. By plotting the critical point as a function of R_{21}, the critical boundary separating *MODE N*1 and *MODE P*1 can be drawn in a state diagram (Figure 2a). It is clear that the R_Y domain of existence of *MODE P*1 widens when R_{21} is increased, but the effect is weak.

3.2 Azimuthal Field; Weak Anchoring; $\chi_A > 0$

The structures of *MODE N*1 and *MODE P*1 remain the same except that now ϕ obeys the condition (18). As the spatial derivative of ϕ is fixed at the boundaries, ϕ does not vanish there. The *NPD* threshold Y_F is found as before by assuming dependence of ϕ on r. For simplicity, the twist anchoring strengths at the two cylinders are assumed equal: $A_{\phi 1} = A_{\phi 2} = A_\phi$, say. From (11) and (18), Y_F can be determined numerically from the condition:

$$
\begin{aligned}
&2a\sqrt{\zeta}\Sigma\cos\left(\sqrt{\zeta}\log(R_{21})\right) - \\
&((k_2 + \Sigma\sigma_2)(k_2 - \Sigma\sigma_1) + \zeta)\sin\left(\sqrt{\zeta}\log(R_{21})\right) = 0\,; \\
&\zeta = \frac{\chi_A}{K_2}Y^2 - 1\,;\ \Sigma = \frac{A_\phi h}{K_2}\,;\ k_2 = \frac{K_2 - K_{24}}{K_2}\,; \\
&\sigma_1 = \frac{2}{R_{21} - 1}\,;\ \sigma_2 = \frac{2R_{21}}{R_{21} - 1}\,.
\end{aligned}
\tag{24}
$$

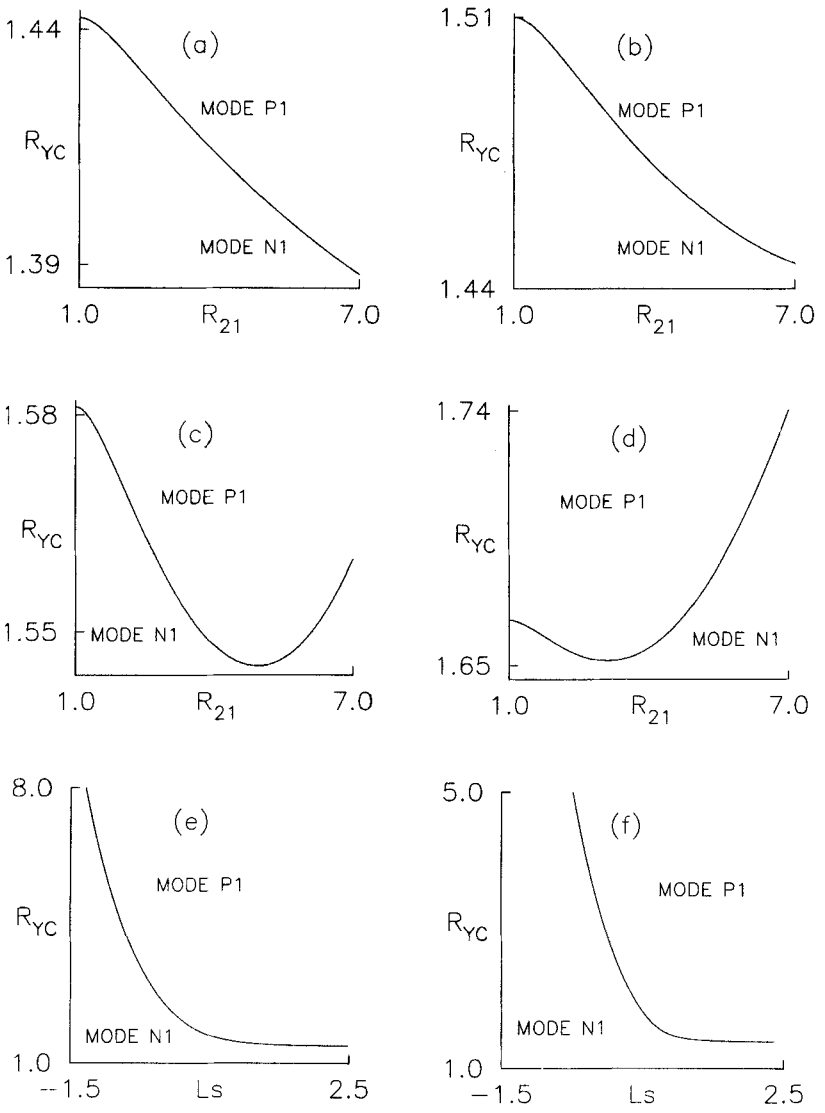

FIGURE 2 Details as in Figure 1. State diagrams containg the critical boundary separating *MODE P*1 and *MODE N*1. R_{YC} is the critical value of the reduced azimuthal **H** and is a function of R_{21} and the dimensionless parameter Σ (24) which measures the twist anchoring strength (when the director anchoring is weak). Figure 2a represents rigid anchoring (section 3.1). Figures 2b – 2d are drawn for Σ = (b) 11.67 (c) 5.85 (d) 3.69. In these cases, Y_F is calculated from (24) and then R_{YC} is computed. The change in shape of the critical boundary with weakening of director anchoring is apparent. In Figures 2e, 2f, R_{21}= 1.02 and 7, respectively. $Ls = \log_{10}(\Sigma)$. Increase in R_{21} curtails the Σ range of existence of *MODE P*1; Figure 2e compares well with the results of Appendix 3 obtained for a flat sample. K_{24} has negligible influence on these results (section 3.2)

The expressions corresponding to $\chi_A Y^2/K_2 < 1$ can be obtained by making ζ negative in (24). Clearly, Y_F becomes a function of Σ and R_{21} for given values of other parameters. In the limit of rigid anchoring, the dimensionless parameter $\Sigma \gg 1$ and (24) reduces to (21). In general, Y_F diminishes with Σ (ie., with a weakening of the director anchoring at the boundaries). For real interfaces [7], A_ϕ takes values in the range 10^{-4} to 10^{-2} erg cm^{-2}. If $h = 100$ μm, Σ should be ~ 1 to 100 for a typical nematic (23).

Let us fix the material parameters as in (23). The boundary conditions involve K_{24} which we assume initially to be zero. *MODE N*1 again involves no flow. Using (19), (11) and (18) it can be shown that $s_A h^2$ is a function of Σ, R_{21} and R_Y provided that Y_F from (24) is employed for calculating the reduced field. Using (19), (11), (13), (16) and (18), it can be proved that $s_P h^2$, Σ, R_{21}, R_Y and Q_Z are related. This implies that R_S and Q_Z can be studied as functions of R_{21}, R_Y and Σ making the results dependent on the product $h\, A_\phi$. The numerical solutions for *MODE N*1 and *MODE P*1 proceed as in Appendix 2 except that we use boundary conditions (16) and (18).

At given R_{21} and Σ, the plots of $R_S$and Q_Z versus R_Y (Figures 3a, 3b) are similar to those contained in Figures 1a, 1b for rigid anchoring. A weakening of the twist anchoring curtails the R_Y range of existence of *MODE P*1. At fixed R_Y and Σ, the variation of parameters with R_{21} is similar to that shown in Figures 1c, 1d; increase of R_{21} is accompanied by an increase in Q_Z and a decrease in R_S; these results have not been presented. At fixed R_{21} and R_Y, Σ can be varied. It is found (Figure 3c, 3d) that both R_S and Q_Z decrease with Σ; weakening of the twist anchoring causes the stripes to broaden. When Σ approaches a lower limit Σ_L, $R_S \to 1$ and $Q_Z \to 0$ showing that for $\Sigma < \Sigma_L$, *MODE N*1 prevails. Higher the R_Y, lower the Σ_L. If R_{21} is raised, the resulting diagrams are similar to Figures 3c, 3d except that Σ_L values are higher; this means, *MODE P*1 is quenched when the anchoring is stronger.

Two sets of critical boundaries can be studied in the present case. Figures 2b-2d show the critical boundaries between *TPDS* and *AR* for different Σ values in the $R_Y - R_{21}$ plane with $R_{21} < 7$. As long as the anchoring is not too weak (Figure 2b). the boundary has the same shape as for rigid anchoring (Figure 2a). One discerns a change in the shape of the boundary when the anchoring is made sufficiently weak (Figures 2c, 2d): it appears that the R_Y range of existence of *MODE P*1 shrinks when $R_{21}$is sufficiently high. A critical boundary can be drawn in the $R_Y - \Sigma$ plane when R_{21} is fixed. Starting with a given Σ, R_Y is diminished from a high value; when R_Y approaches the lower limit R_{YC}, *MODE P*1 gets suppressed. The plots of R_{YC} versus Σ for two R_{21} values yield Figures 2e, 2f. Increase of R_{21} results in *MODE P*1 being suppressed at a higher Σ. In Fig-

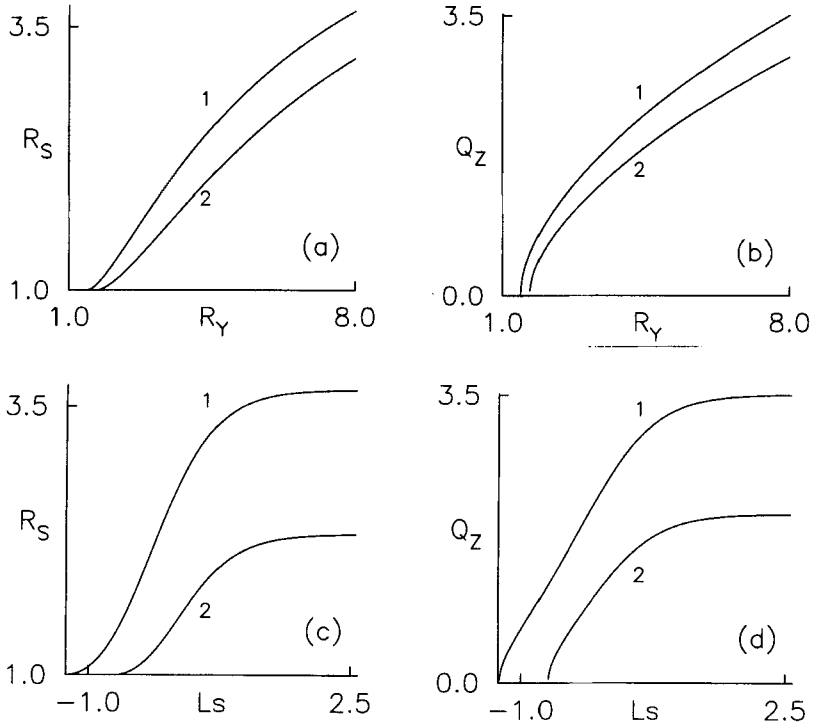

FIGURE 3 Details as in Figures 1 and 2. $R_{21} = 1.02$. The director anchoring is weak, with Σ being a measure of the twist anchoring strength at either boundary. R_S and Q_Z have the same meaning pertaining to *MODE P*1 and *MODE N*1, but R_Y is defined using Y_F calculated from (24). Figures 3a, 3b: variations of R_S and Q_Z with R_Y for Σ = (1) 369 (2) 3.69. Figures 3c, 3d: plots of R_S and Q_Z versus $L_S = \log_{10}(\Sigma)$. $R_{21} = 1.02$. R_Y = (1) 8 (2) 4. At a given R_Y, *MODE P*1 gets quenched in favour of *MODE N*1 when the anchoring is weakened sufficiently (section 3.2). Results for $R_{21} = 1.02$ compare well with those obtained for the twist geometry in a flat sample ([11]; see Appendix 3)

ures 3c, 3d, R_{21} is chosen close to unity; hence, these results should be comparable to those obtained for twist geometry in a flat sample ([11]; see Appendix 3 for more details). So far K_{24} has been assumed to be zero. It is found that even when K_{24} takes its maximum permitted value [23], the results for dimensionless growth rate and *PWV* do not change appreciably.

3.3 Axial Field; Rigid Anchoring; $\chi_A < 0$

In this case, **H** (4) is constant in the gap as opposed to the two earlier sections where the field strength drops off as we move from the inner to the outer cylin-

der. This should certainly affect how the different quantities depend on the geometric parameters; in particular, a change in the nature of scaling can be expected. Secondly, **H** couples to both θ and ø via destabilizing torques; hence, both distortions may have to be studied. The task of comparing the behaviour of this material with a nematic having positive χ_A becomes easier if we adopt the parameters (23) with the sign of χ_A reversed. The *NPD* threshold is studied by ignoring dynamic effects and assuming dependence of perturbations on *r*. The θ (splay) and ø (twist) modes get decoupled. As $K_1 > K_2$, the threshold for ø (viz., H_F) is lower than that for θ; H_F is determined numerically by solving (11) with (20). The reduced field is defined as

$$R_z = \frac{H_z}{H_F}.$$

AR is associated with ø which does not couple with flow. The growth rate of *AR*, s_A, can be determined from (11) and (20) to be

$$s_A = -\frac{\chi_A H_F{}^2}{\gamma_1}\left(R_z{}^2 - 1\right).$$

Independently, we have the aperiodic θ mode coupled to the back-flow υ_z [8]. At a given **H**, the $\theta - \upsilon_z$ mode grows more slowly than the ø mode for parameters (23); hence, we study only *AR* associated with ø. *TPDS* with the attributes of *MODE P*1 (section 3.1) can be studied by fixing the dependence of *r*, *z* and *t* for the perturbations. Again, ø couples with ω if periodicity along *z* is assumed. Using (11), (13), one numerically computes R_S, the dimensionless growth rate of *MODE P*1 relative to that of *AR* and Q_Z, the corresponding dimensionless *PWV*.

The variations of different parameters shown in Figure 4 bear some resemblance to those of Figure 1. For instance, *TPDS* disappears below a critical reduced field $R_Z = R_{ZC}$ when R_{21} is fixed, Figures 4a, 4b). At a given R_Z, the wavevector, Q_Z increases with R_{21} (Figures 4c, 4d). But there are some important differences. It is seen that (Figures 4a, 4b) R_S is independent of R_{21} but depends only on R_Z. The reduced critical field $R_{ZC} \approx 1.445$ regardless of R_{21}; this value is close to the critical field calculated for a flat sample (Appendix 3). Hence, the counterpart of Figure 2a would carry the critical boundary in the form of a horizontal line at $R_{ZC} \approx 1.445$. This qualitative difference between the effects of the azimuthal and axial fields stems from the different spatial variations of the two fields. As χ_A is negative, **H** produces a destabilizing torque on θ which can, in principle, result in a convective *TPDS* involving periodically varying υ_r and υ_z. This mode can be expected to grow more slowly than *MODE P*1 and is, therefore, ignored.

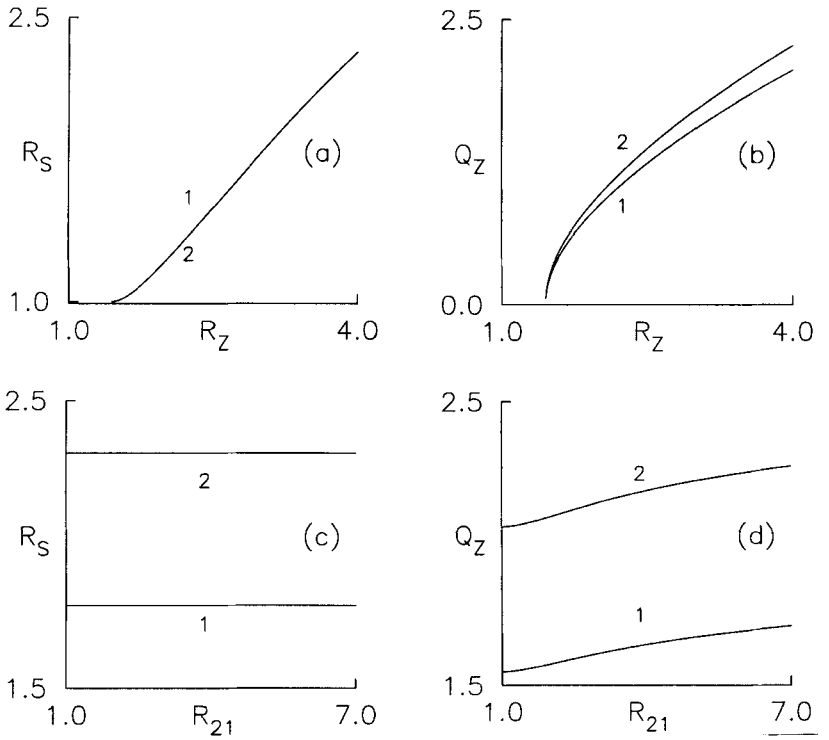

FIGURE 4 Axially aligned nematic (1) subjected to the action of axial **H** (4). The director is rigidly anchored at the boundaries. Material parameters are (23) except that χ_A has a negative sign. R_S and Q_Z are defined as in Figure 1 while R_Z, the reduced field, is calculated as in section 3.3. Figures 4a, 4b: plots of R_S and Q_Z versus R_Z at R_{21} = (1) 1.02 (2) 7. R_S as well as the critical point, R_{ZC}, are independent of R_{21}. Figures 4c, 4d: plots of R_S and Q_Z as functions of R_{21} for R_Z = (1) 3 (2) 4. These support the conclusions of Figures 4a, 4b (see section 3.3). Compare with Figure 1. The effect of an azimuthal **H** on a material with positive χ_A is similar except for some differences (see also section 3.1)

3.4 Radial Field; Rigid Anchoring; $\chi_A > 0$

These results are briefly stated for the sake of completeness [20] as the radial **H** is the counterpart of **H** acting normal to the substrates of a flat sample. With **H** given by (6), ϕ is of no relevance for the static and dynamic modes studied in earlier sections. The *NPD* threshold, X_F, is calculated from (10) and (20) by assuming that θ depends only on r. The expression for X_F is given by (21) with K_2 replaced by K_1. The reduced field is defined as

$$R_X = \frac{X}{X_F}.$$

The *AR* (**MODE N2**) involves θ coupling with the back-flow v_z [8]. The coupling is weak as it occurs via μ_3 [26]. With a time dependence of the form $\exp(s\,t)$, (10) and (12) yield two coupled *ODE*s to be solved numerically; the growth rate, s_A, of *MODE N2* is obtained thus. Using (23) it is verified that $s_A \geq 0$ when $R_X \geq 1$. The periodic mode (**MODE P2**) is associated with θ, v_z and the convective component, v_r which (along with p) have the dependence,

$$(\theta\,,\ v_r\,,\ v_z\,,\ p) = (T(r)\cos(q\,z)\ ,\ V_1(r)\sin(q\,z)\ ,\ V_3(r)\cos(q\,z)\ ,\ p_a(r)\sin(q\,z))\exp(s\,t)\,.$$

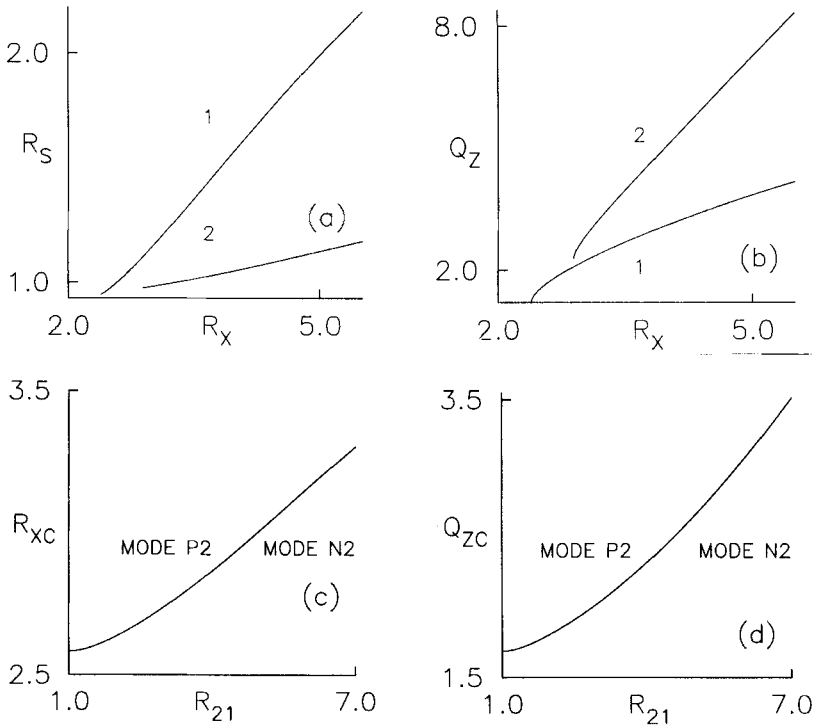

FIGURE 5 Axially aligned nematic (1) subjected to the action of radial **H** (6). Material parameters are (23) and the director is rigidly anchored at the substrates. R_X, R_S and Q_Z are defined as in section 3.4. R_S is the ratio of the growth rates of *MODE P2* and *MODE N2*, respectively. Figures 5a, 5b: plots of R_S and Q_Z versus R_Z at $R_{21} = (1)\ 1.02\ (2)\ 7$. For $R_X < R_{XC}$, *MODE P2* is not favourable,but $Q_Z = Q_{ZC}$ is non-zero. Figures 5c, 5d: plots of R_{XC} and Q_{ZC} as functions of R_{21}. Increase of R_{21} curtails the R_X range of existence of *MODE P2*. This trend is opposite to what is found for *MODE P1* with an azimuthal field (Figure 2b; see section 3.4)

The convective nature of this flow is clear as θ and v_z are out of phase with respect to v_r along $z - a$ requirement that not only fulfils the equation of continu-

ity (9) but also establishes a relationship between υ_r and υ_z. Using (12) and (14), p_a can be eliminated and the resulting system of *ODE*s solved numerically. At sufficiently high R_X, the growth rate, s_P, of *MODE P2* can be determined as the extremum of the neutral stability curve occurring at a dimensionless *PWV*, Q_Z; s_P is found to be higher than s_A. This is due to the well known reason [10, 22] that at a sufficiently elevated periodicity wavevector, the effective viscosity associated with a convective, transient flow can become less than that associated with the non-periodic back-flow. It is sufficient to study the reduced growth rate, R_S, and Q_Z as functions of R_X and R_{21}.

The variations of R_S and Q_Z with R_X (Figures 5a, 5b) are similar in some respects to those of corresponding quantities in Figures 1a, 1b; *MODE N2* becomes more favourable than *MODE P2* when R_X falls below a lower limit, R_{XC}. At $R_{21} = 1.02$, $R_{XC} \approx 2.59$ (see section 4.2). Increase in R_{21} lowers the growth rate of *MODE P2* relative to that of MODE *N2* but raises Q_Z; at fixed h, the stripes become sharper when R_{21} is enhanced. However, there are some differences between the behaviours of *MODE P2* and *MODE P1*. When $R_S \to 1$, Q_Z is not zero but takes a value Q_{ZC} which is a function of R_{21}. Regarding Q_Z as an order parameter characterizing the striped phase, we can state that the extinction of *TPDS* is discontinuous. By systematically varying R_{21}, R_{XC} and Q_{ZC} can be determined (Figures 5c, 5d). Secondly. at a fixed R_{21}, R_{XC} (Figure 5c) is higher than R_{YC} for *MODE P1* (Figure 2a). While *MODE P1* involves periodic flow in the $r\psi$ plane. *MODE P2* is associated with a convective, periodic flow in the rz plane which has a higher rate of energy dissipation than that of *MODE P1*. The third point is that R_{XC} increases with R_{21}; hence, the R_X range of existence of *MODE P2* becomes narrower with an increase of R_{21}; this is opposed to the result obtained for *MODE P1* (compare Figures 2a and 5c).

3.5 "Oblique" Field; Rigid Anchoring; $\chi_A > 0$

We briefly study this configuration which involves the effect of **H** with r and ψ components and zero z component:

$$\mathbf{H} = \left(\frac{X}{r}, \frac{Y}{r}, 0\right) = \left(\frac{G\cos(\lambda)}{r}, \frac{G\sin(\lambda)}{r}, 0\right),$$

where $0 \leq \lambda \leq \pi/2$ without loss of generality. **H** goes over from radial to azimuthal as λ is varied from 0 to $\pi/2$. Hence, the extent of discontinuity in *PWV* at the point of suppression of *TPDS* should decrease to zero when λ reaches the upper limit of its range. At general λ, θ and ϕ get coupled in (10) and (11) as the

cross coupling term m_2 is non-zero. With r dependence, the *NPD* threshold G_F for the twist – splay distortion can be written down by using the method given in [15]:

$$G_F^2 = \frac{K_1 K_2}{\chi_A \left(K_1 \sin^2(\lambda) + K_2 \cos^2(\lambda)\right)} \left[1 + \left(\frac{\pi}{\ln(R_{21})}\right)^2\right]. \quad (25)$$

The reduced field can be defined as $R_G = G/G_F$. With a dependence on r and t, the growth rate s_A of *AR* (**MODE N3**) is computed from (10)-(12). *MODE N*3 is described by ϕ, θ and the back-flow υ_z. *TPDS* with z periodicity (**MODE P3**) involves all perturbations for which a closed solution is obtained by combining the assumptions made for *MODE*s *P*1 and *P*2 (sections 3.1 and 3.4):

$$(\theta, \phi, \upsilon_z) = (T(r), P(r), V_3(r)) \cos(q z) \exp(s t)$$
$$(\upsilon_r, \omega, p) = (V_1(r), \Omega(r), p_a(r)) \sin(q z) \exp(s t).$$

Thus, θ, ϕ and υ_z are in phase with one another with respect to z variation; so are υ_r, ω and p. However, the perturbations of one set are out of phase with respect to those of the other set. The growth rate, s_p, and the dimensionless *PWV*, Q_Z of *MODE P*3 are computed by solving (10) – (14); Q_Z and R_S are studied as functions of R_G, R_{21} and λ. Suppose R_{21} is fixed. When λ is close to zero, the variations of R_S and Q_Z with R_G are similar to those exhibited by *MODE P*2 (Figure 5a. 5b); *MODE P*3 gets extinguished discontinuously when R_G falls below a lower limit, R_{GC}, at which $Q_Z = Q_{ZC}$ does not vanish. When λ approaches the opposite limit, $\pi/2$, the curves resemble those in Figures 1a, 1b for *MODE P*1; the discontinuity at the extinction point is less pronounced with Q_{ZC} taking very low values. These diagrams are left out. The state diagrams (Figure 6) describe the effect of λ and R_{21} on the occurrence of *MODE P*3.

The critical boundaries can be drawn in two separate planes. First, R_{21} is fixed. R_{GC} and Q_{ZC} are studied as functions of λ. Suppose λ is close to zero. Then, Q_{ZC} is non-zero. When λ is increased, R_{GC} and Q_{ZC} diminish continuously (Figures 6a, 6b) till Q_{ZC} vanishes as $\lambda \to \pi/2$; in the same limit, R_{GC} takes a lower limiting value corresponding to R_{YC} of *MODE P*1 (section 3.1). Essentially, the transition from *TPDS* to *AR* remains discontinuous but the extent of discontinuity diminishes as the azimuthal component of **H** increases.

More interesting is the critical boundary in the $R_G - R_{21}$ plane. It is seen (Figures 2a, 5c) that the average slope of the critical boundary reverses sign when λ is taken from one limit to the other. In addition, the variation of R_{YC} with R_{21} is weak (Figure 2a) compared to that of R_{XC} (Figure 5c). A small change in λ from its limits does not appreciably alter the shape of the critical boundary. Thus,

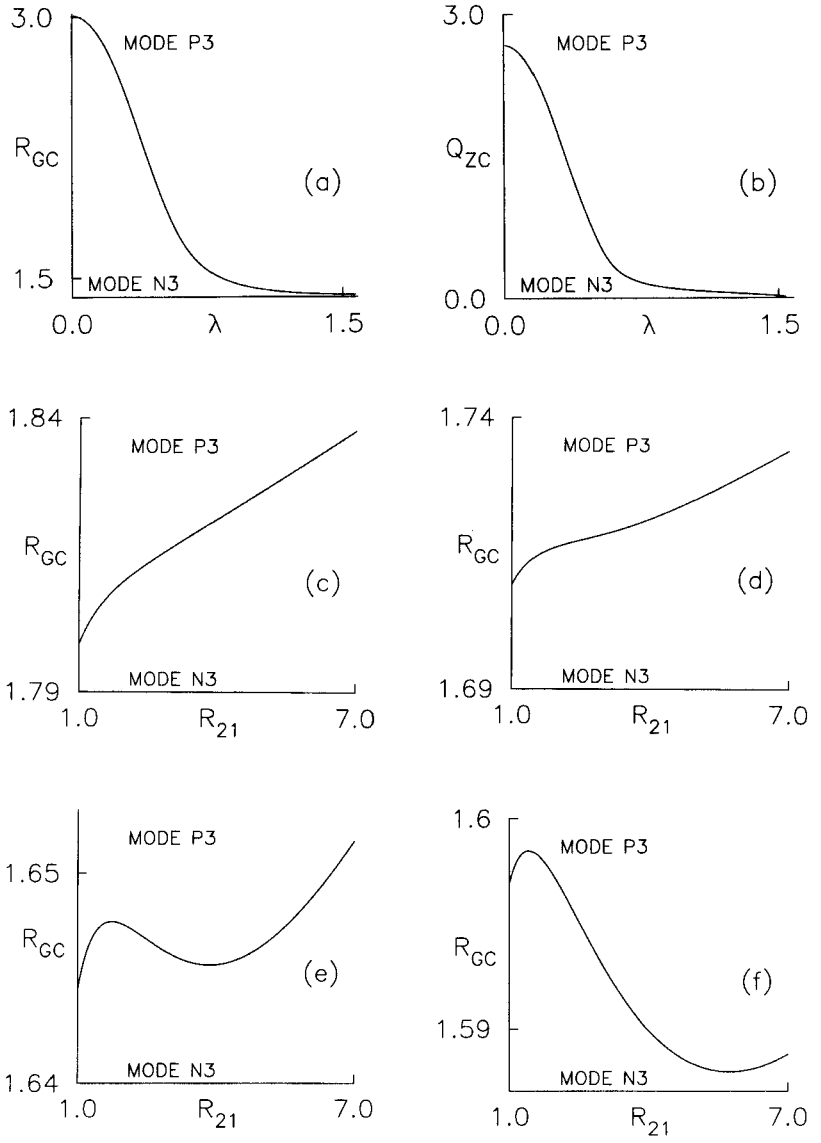

FIGURE 6 Axially aligned nematic (1) subjected to the action of oblique **H.** Rigid anchoring of the director at the boundaries. Parameters as in (23). The Freedericksz threshold is (25). Plots of cut-off reduced field, R_{GC} below which the *TPDS* (*MODE P*3) gets quenched. Q_{ZC}, the wavevector at the quenching point, is non-zero showing that the transition to the aperiodic *MODE N*3 is discontinuous. Figures 6a, 6b: Plots of R_{GC} and Q_{ZC} versus magnetic tilt, λ, at $R_{21} = 5$. Figures 6c – 6f: Variation of R_{GC} with R_{21} for λ = (c) 0.55 (d) 0.6 (e) 0.65 (f) 0.7 radian. The reversal in the sign of the average slope of the critical boundary is evident (section 3.5)

the curve for $\lambda = 0.3$ radian is similar to that of Figure 5c; the critical boundary at $\lambda = 1.0$ is similar in shape to that of Figure 2a. The changeover, therefore, occurs in mid-range. Figures 6c – 6f contain plots of R_{GC} versus R_{21} for four, closely spaced magnetic tilts. The reversal in average slope of the critical boundary occurs over a small λ range. The variation of Q_{ZC} with R_{21} has not been presented; Q_{ZC} diminishes continuously with R_{21} at all λ.

4. AZIMUTHAL INITIAL ORIENTATION

With $\mathbf{n_0}$ given by (2), the equilibriun pressure p_0 is a function of r (Appendix 1) due to a global curvature deformation. Under perturbation,

$$\mathbf{n} = \left(\theta, 1 - \frac{\theta^2 + \phi^2}{2}, \phi\right)$$

and $\mathbf{V}$ is given by (8). The governing equations are (9) and

$$K_1\frac{\partial^2\theta}{\partial r^2} + \frac{K_3}{r^2}\frac{\partial^2\theta}{\partial\psi^2} + K_2\frac{\partial^2\theta}{\partial z^2} + \frac{K_1}{r}\frac{\partial\theta}{\partial r} + \frac{\theta}{r^2}(m_1 - m_4 + K_3 - K_1)$$
$$- \gamma_1\frac{\partial\theta}{\partial t} + \frac{m_5}{r}\phi + \frac{K_2 - K_3}{r}\frac{\partial\phi}{\partial z} + (K_1 - K_2)\frac{\partial^2\phi}{\partial r\partial z}$$
$$- \frac{\mu_2}{r}\frac{\partial v_r}{\partial\psi} - \mu_3 r\frac{\partial\omega}{\partial r} = 0 \tag{26}$$

$$K_2\frac{\partial^2\phi}{\partial r^2} + \frac{K_3}{r^2}\frac{\partial^2\phi}{\partial\psi^2} + K_1\frac{\partial^2\phi}{\partial z^2} + \frac{K_2}{r}\frac{\partial\phi}{\partial r} + \frac{\phi}{r^2}(2K_3 - K_2 - m_4)$$
$$- m_3\phi - \gamma_1\frac{\partial\phi}{\partial t} + \frac{m_5}{r}\theta + \frac{(K_1 - 2K_2 + K_3)}{r}\frac{\partial\theta}{\partial z}$$
$$+ (K_1 - K_2)\frac{\partial^2\theta}{\partial r\partial z} - \frac{\mu_2}{r}\frac{\partial v_z}{\partial\psi} - \mu_3 r\frac{\partial\omega}{\partial z} = 0 \tag{27}$$

$$\mu_4\frac{\partial^2 v_r}{\partial r^2} + \frac{\eta_C}{r^2}\frac{\partial^2 v_r}{\partial\psi^2} + \eta_A\frac{\partial^2 v_r}{\partial z^2} + \frac{\mu_4}{r}\frac{\partial v_r}{\partial r} - \frac{2\nu_1}{r^2}v_r$$
$$+ \eta_D\frac{\partial^2\omega}{\partial r\partial\psi} - \frac{2\nu_1}{r}\frac{\partial\omega}{\partial\psi} + \eta_A\frac{\partial^2 v_r}{\partial r\partial z}$$
$$+ \frac{\mu_2}{r}\frac{\partial^2\theta}{\partial\psi\partial t} + \frac{K_3}{r^2}\frac{\partial^2\theta}{\partial r\partial\psi} - \frac{2K_3}{r^3}\frac{\partial\theta}{\partial\psi} = \frac{\partial p}{\partial r} + \rho\frac{\partial v_r}{\partial t} \tag{28}$$

$$\eta_B r\frac{\partial^2\omega}{\partial r^2}+\frac{(2\nu_1)}{r}\frac{\partial^2\omega}{\partial\psi^2}+\eta_B r\frac{\partial^2\omega}{\partial z^2}+(\eta_D+2\eta_B)\frac{\partial\omega}{\partial r}+$$
$$\frac{(2\nu_1+\eta_C)}{r^2}\frac{\partial v_r}{\partial\psi}+\frac{\eta_D}{r}\frac{\partial^2 v_r}{\partial r\partial\psi}+\frac{\eta_D}{r}\frac{\partial^2 v_z}{\partial\psi\partial z}+\frac{(K_1-K_2)}{r}\frac{\partial^2\phi}{\partial r\partial z}$$
$$+\mu_3\frac{\partial^2\phi}{\partial z\partial t}+\frac{(K_2-K_3)}{r^2}\frac{\partial\phi}{\partial z}+\frac{m_5}{r^2}\phi+\frac{K_1}{r}\frac{\partial^2\theta}{\partial r^2}+\frac{2K_3}{r^3}\frac{\partial^2\theta}{\partial\psi^2}$$
$$+\frac{K_2}{r}\frac{\partial^2\theta}{\partial z^2}+\mu_3\frac{\partial^2\theta}{\partial r\partial t}+\frac{K_1}{r^2}\frac{\partial\theta}{\partial r}+\frac{(\mu_2+\mu_3)}{r}\frac{\partial\theta}{\partial t}$$
$$+\frac{(K_3-K_1+m_1-m_4)}{r^3}\theta=\frac{1}{r}\frac{\partial p}{\partial\psi}+\rho r\frac{\partial\omega}{\partial t} \tag{29}$$

$$\eta_A\frac{\partial^2 v_z}{\partial r^2}+\frac{\eta_C}{r^2}\frac{\partial^2 v_z}{\partial\psi^2}+2\eta_A\frac{\partial^2 v_z}{\partial z^2}+\frac{\eta_A}{r}\frac{\partial v_z}{\partial r}$$
$$+\eta_A\frac{\partial^2 v_r}{\partial r\partial z}+\frac{\eta_A}{r}\frac{\partial v_r}{\partial z}+\eta_D\frac{\partial^2\omega}{\partial\psi\partial z}+\frac{\mu_2}{r}\frac{\partial^2\phi}{\partial\psi\partial t}$$
$$+\frac{K_3}{r^2}\frac{\partial^2\theta}{\partial\psi\partial z}=\frac{\partial p}{\partial z}+\rho\frac{\partial v_z}{\partial t} \tag{30}$$

$$m_5=\chi_A H_z X. \tag{31}$$

These differ from their counterparts (10) – (14) for the axial $\mathbf{n_0}$ in the following way. The linear momentum balance equations (28) – (30) contain elastic as well as magnetic contributions. By using the torque equations (26) – (27), the elastic and magnetic terms can be eliminated from (28) – (30) when p is removed through differentiation. At a time, the effect of one of the three **H's** of (4) – (6) can be studied; an "oblique" **H** having r and z components can also be considered. If the anchoring is weak (17), the boundary conditions for θ and ø are given by (18) with

$$\tau_\theta = K_1\frac{\partial\theta}{\partial r}+\frac{(K_1-K_3)}{r}\theta+(K_1-K_{24})\frac{\partial\phi}{\partial z};$$
$$\tau_\phi = K_2\frac{\partial\phi}{\partial r}+\frac{(K_{24}-K_2)}{r}\phi+(K_{24}-K_2)\frac{\partial\theta}{\partial z}.$$

The expressions for τ_θ and τ_ϕ are distinctly different from those of section 3 derived for the axial $\mathbf{n_0}$. We consider only rigid anchoring.

4.1 Axial Field; $\chi_A > 0$

With **H** given by (4) and dependence only on r, the twist distortion ø can occur above the *NPD* threshold, H_F, which is numerically computed from (27). Defin-

ing the reduced magnetic field R_Z as in section 3.3, dynamic reorientation can be expected for $R_Z > 1$. For *AR*, the backflow ω couples with θ but both these perturbations damp out as θ has no driving magnetic torque. In this geometry again, the twist ϕ does not couple with flow and the growth rate, s_A, of *AR* (**MODE N4**) is given by an expression identical to the one in section 3.3 except that the negative sign is removed. The *TPDS* (**MODE P4**) that is analogous to that studied in [27] for the twist geometry in a flat sample requires the perturbations to depend on r, ψ and t. *MODE P4* has ϕ coupling with v_z such that

$$(\phi, v_z) = (P(r)\cos(b\psi), V_3(r)\sin(b\psi))\exp(st).$$

For perturbations to be single valued under the transformation $\psi \rightarrow \psi + 2\pi$, b must be an integer. Substitution in (27) and (30) results in a pair of coupled *ODE*s which are solved numerically to calculate s as a function of b, $s = s(b)$, at fixed values of other parameters. In the limit of vanishing b, $s(b) \rightarrow s_A$. When R_Z is high enough (**H** strong enough), increase of b from a low value results in an increase of $s(b)$. When $b = b_P$, s becomes a maximum at $s_P = s(b_P)$. We take s_P to be the instantaneous growth rate of *MODE P*4 and assume that b_P is the instantaneous *PWV* of modulation along the ψ coordinate curve (in other words, b_P is a measure of the number of domains that can form at the time of impressing **H**). The formation of *MODE P*4 should be accompanied by the appearance of bright and dark stripes parallel to the axis of the cylinders. One studies R_S and b_P as functions of R_Z and R_{21}.

Plots of R_S and b_P are shown in Figure 7 and bear some qualitative similarity to the plots of corresponding quantities in Figure 4. When R_Z is high enough (Figures 7a, 7b), the number of domains that form is also high as is the growth rate of *MODE P*4 with respect to that of *MODE N*4. When R_Z is reduced in small steps, R_S diminishes continuously but the number of domains changes discontinuously. When R_Z approaches a lower limit R_{ZC}, b_P decreases to zero and R_S to unity so that for $1 < R_Z < R_{ZC}$, only *MODE N*4 can develop. The transition from *MODE P*4 to *MODE N*4 is again one of second order showing that the amplitude of v_z is proportional to the order parameter, b_P (compare with Figures 1a, 1b, 4a, 4b). Small changes in R_{21} cause large variations in b_P at a given R_Z but R_S and R_{ZC} do not depend strongly on R_{21}. As in section 3.3, $R_{ZC} \approx 1.445$ (Appendix 3). Figures 7c and 7d which represent the plots of relevant parameters with R_{21} at fixed R_Z reflect the above results. A small increase of R_{21} causes little change in R_S but a perceptible decrease in b_P (diminution in the number of domains); the rate of decrease of domains is high (or low) in the low (or high) R_{21} range.

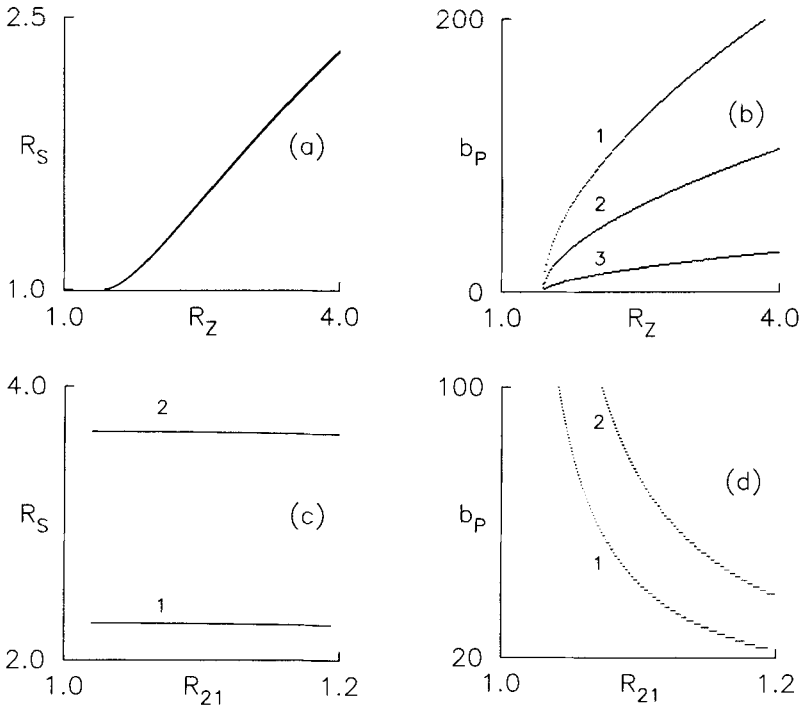

FIGURE 7 Azimuthally aligned nematic (2) subjected to the action of axial **H** (4). Rigid anchoring of the director at the boundaries. *TPDS* with azimuthal modulation (*MODE P*4) may develop with an integral wavevector b_P instead of the aperiodic *MODE N*4 if H is strong enough. The results correspond to the parameters (23). The dimensionless field, R_Z and the reduced growth rate, R_S are defined in section 4.1. (a,b) Plots of R_S and b_P as functions of R_Z for $R_{21} = (1)$ 1.02 (2) 1.04 (3) 1.15. The dependence of R_S on R_{21} is weak; hence, the absence of numbering in (a). (c,d) Variations of R_S and b_P with R_{21}, the ratio of cylinder radii, at $R_Z = (1)$ 3.9 (2) 8. The number of domains varies in discontinuous jumps with continuous changes of R_Z and R_{21}

4.2 Radial Field; $\chi_A > 0$

When **H** is radial (6), it couples with θ so that the perturbation set containing ϕ is not relevant in this section. The *NPD* threshold X_F is obtained from (26) by assuming a dependence on only r and ignoring the velocity components:

$$X_F^2 = \frac{K_1}{\chi_A}\left[\left(\frac{\pi}{\ln(R_{21})}\right)^2 + 1 - \frac{K_3}{K_1}\right]. \tag{32}$$

If K_3/K_1 or R_{21} is sufficiently large, X_F of (32) becomes imaginary showing that the uniform orientation (2) is unstable against aperiodic perturbations. We do not consider such a material or geometric parameter. The reduced field R_X is

defined as in section 3.4. Then dynamic reorientation can be expected to occur if $R_X > 1$. The *AR* (**MODE N5**) is associated with θ and ω. At a given R_X, the growth rate, s_A, of *MODE N*5 is found numerically from (26), (29). At sufficiently high R_X, *TPDS* (**MODE P5**) analogous to that studied in [10,22] for flat samples can be expected with an azimuthal modulation. Such a solution represents a convective flow in the $r - \psi$ plane involving v_r and ω if these velocity components are out of phase with respect to each other for azimuthal variation.

The substitution

$$(\theta\,,\ v_r\,,\ \omega\,,\ p) = (T(r)\cos(b\psi)\ ,\ V_1(r)\sin(b\psi)\ ,\ \Omega(r)\cos(b\psi)\ ,\ p_a(r)\sin(b\psi))\exp(st)$$

provides a closed solution of (9), (26), (28) and (29) with the growth rate, s, becoming a function of b. At sufficiently high R_X, the maximum growth rate, $s_P = s(b_P)$ occurs at $b = b_P$. Again, R_S and b_P are functions of R_{21} and R_X for a given material. Figure 8 contains the relevant plots. The qualitative nature of the variation is similar to that represented in Figure 5. For small changes in R_{21}, R_S is hardly affected but b_P displays considerable variation. As in section 4.1, b_P changes only in steps of unity. *MODE P*5 gets quenched discontinuosly when R_X diminishes below a limit R_{XC}; $R_{XC} \approx 2.59$ for the parameters chosen (see section 3.4).

5. RADIAL INITIAL ORIENTATION

When $\mathbf{n_0}$ is given by (3), we have the counterpart of the homeotropic alignment in flat geometry but with a difference. In a flat sample, there exists no unique direction of periodicity normal to the homeotropic $\mathbf{n_0}$. Consider now perturbations that possess periodicity normal to the radial $\mathbf{n_0}$. The curvature of the cylinders ensures that periodicity along the azimuthal direction is distinctly different from that along the axial direction. As seen already, the azimuthal modulation is restricted by the wavevector having to assume integral values. Due to the global curvature in the radial $\mathbf{n_0}$, the equilibrium pressure p_o depends on r (Appendix 1). For small perturbations, $\mathbf{V}$ is given by (8) and

$$\mathbf{n} = \left(1 - \frac{\phi^2 + \theta^2}{2}, \phi, \theta\right).$$

Both the distortions ø and θ correspond to a bend when they depend only on r. But as they occur in two different, orthogonal planes, their elastic energies will be different; they should also couple differently with viscous and magnetic torques. The equation of continuity is (9) and the remaining governing equations are

$$K_3\frac{\partial^2\phi}{\partial r^2}+\frac{K_1}{r^2}\frac{\partial^2\phi}{\partial\psi^2}+K_2\frac{\partial^2\phi}{\partial z^2}+\frac{K_3}{r}\frac{\partial\phi}{\partial r}+\frac{\phi\,(m_4-m_1+K_1-K_3)}{r^2}-$$
$$\gamma_1\frac{\partial\phi}{\partial t}+\frac{(K_1-K_2)}{r}\frac{\partial^2\theta}{\partial\psi\partial z}+\frac{m_6}{r}\theta-\frac{\mu_3}{r}\frac{\partial v_r}{\partial\psi}-\mu_2\,r\,\frac{\partial\omega}{\partial r}=0 \tag{33}$$

$$K_3\frac{\partial^2\theta}{\partial r^2}+\frac{K_2}{r^2}\frac{\partial^2\theta}{\partial\psi^2}+K_1\frac{\partial^2\theta}{\partial z^2}+\frac{K_3}{r}\frac{\partial\theta}{\partial r}+\frac{\theta\,(K_1-m_1)}{r^2}-$$
$$\gamma_1\frac{\partial\theta}{\partial t}-m_3\theta+\frac{(K_1-K_2)}{r}\frac{\partial^2\phi}{\partial\psi\partial z}+\frac{m_6}{r}\phi-$$
$$\mu_3\frac{\partial v_r}{\partial z}-\mu_2\frac{\partial v_z}{\partial r}=0 \tag{34}$$

$$2\nu_1\frac{\partial^2 v_r}{\partial r^2}+\frac{\eta_B}{r^2}\frac{\partial^2 v_r}{\partial\psi^2}+\eta_B\frac{\partial^2 v_r}{\partial z^2}+\frac{2\nu_1}{r}\frac{\partial v_r}{\partial r}-\frac{\mu_4}{r^2}v_r$$
$$+\eta_D\frac{\partial^2\omega}{\partial r\partial\psi}-\frac{\mu_4}{r}\frac{\partial\omega}{\partial\psi}+\eta_D\frac{\partial^2 v_z}{\partial r\partial z}+\frac{(K_{24}-K_1)}{r}\frac{\partial^2\theta}{\partial r\partial z}$$
$$+\mu_3\frac{\partial^2\theta}{\partial z\partial t}+\frac{(K_1-K_{24})}{r^2}\frac{\partial\theta}{\partial z}-\frac{K_1}{r^2}\frac{\partial^2\phi}{\partial r\partial\psi}$$
$$+\frac{2K_1}{r^3}\frac{\partial\phi}{\partial\psi}+\frac{\mu_3}{r}\frac{\partial^2\phi}{\partial\psi\partial t}=\frac{\partial p}{\partial r}+\rho\frac{\partial v_r}{\partial t} \tag{35}$$

$$\frac{\eta_D}{r}\frac{\partial^2 v_r}{\partial r\partial\psi}+\frac{(2\eta_A+\eta_B)}{r^2}\frac{\partial v_r}{\partial\psi}+\eta_C\,r\,\frac{\partial^2\omega}{\partial r^2}+\frac{\mu_4}{r}\frac{\partial^2\omega}{\partial\psi^2}$$
$$+(2\eta_C+\eta_D)\frac{\partial\omega}{\partial r}+\eta_A\,r\,\frac{\partial^2\omega}{\partial z^2}+\frac{\eta_A}{r}\frac{\partial^2 v_z}{\partial\psi\partial z}+\mu_2\frac{\partial^2\phi}{\partial r\partial t}$$
$$+\frac{(\mu_2+\mu_3)}{r}\frac{\partial\phi}{\partial t}-\frac{K_3}{r^2}\frac{\partial\phi}{\partial r}+\frac{(K_3-K_1+m_1-m_4)}{r^3}\phi$$
$$-\frac{K_3}{r}\frac{\partial^2\phi}{\partial r^2}-\frac{2K_1}{r^3}\frac{\partial^2\phi}{\partial\psi^2}-\frac{K_2}{r}\frac{\partial^2\phi}{\partial z^2}-\frac{m_6}{r^2}\theta$$
$$+\frac{(K_2-2K_1+K_{24})}{r^2}\frac{\partial^2\theta}{\partial\psi\partial z}=\frac{1}{r}\frac{\partial p}{\partial\psi}+\rho\,r\,\frac{\partial\omega}{\partial t} \tag{36}$$

$$\eta_D\frac{\partial^2 v_r}{\partial r\partial z}+\frac{\eta_D}{r}\frac{\partial v_r}{\partial z}+\eta_A\frac{\partial^2\omega}{\partial\psi\partial z}+\eta_C\frac{\partial^2 v_z}{\partial r^2}+\frac{\eta_C}{r}\frac{\partial v_z}{\partial r}$$
$$+\frac{\eta_A}{r^2}\frac{\partial^2 v_z}{\partial\psi^2}+\mu_4\frac{\partial^2 v_z}{\partial z^2}-\frac{K_1}{r^2}\frac{\partial^2\phi}{\partial\psi\partial z}+\mu_2\frac{\partial^2\theta}{\partial r\partial t}$$
$$+\frac{(K_{24}-K_1)}{r}\frac{\partial^2\theta}{\partial z^2}+\frac{\mu_2}{r}\frac{\partial\theta}{\partial t}=\frac{\partial p}{\partial z}+\rho\frac{\partial v_z}{\partial t} \tag{37}$$

$$m_6=\chi_A Y H_z. \tag{38}$$

It may be noted that the linear momentum balance equations (35) – (37) contain terms proportional to the surface elastic constant K_{24}. When p is eliminated from (35) – (37), these terms vanish. Hence, K_{24} does not determine the dynamics of an incompressible nematic which obeys the no-slip condition (16). If the fluid can slip at the boundaries, the total stress tensor assumes definite values depending upon the surface viscosity, etc. In such a case, the boundary conditions on **V** may be affected by K_{24}; we do not consider this possibility. For weak anchoring, the boundary conditions for the director are (18) with

$$\tau_\phi = K_3 \frac{\partial \phi}{\partial r} + \frac{(K_3 - K_1)}{r}\phi\,; \quad \tau_\theta = K_3 \frac{\partial \theta}{\partial r} + \frac{(K_{24} - K_1)}{r}\theta.$$

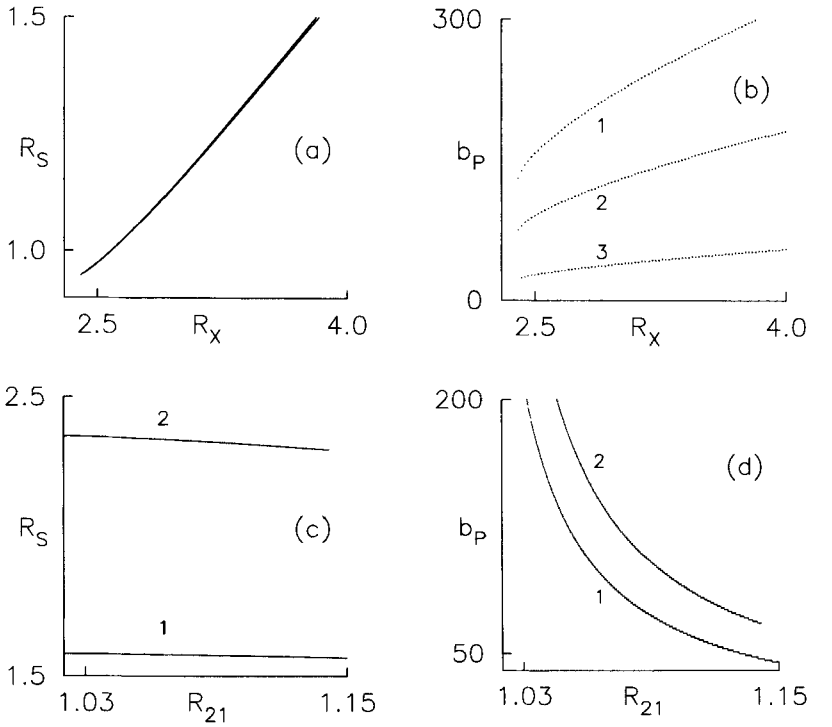

FIGURE 8 Azimuthally aligned nematic with parameters (23) under the action of radial **H** (6). Rigid anchoring at the boundaries. R_X the reduced field potential is calculated with respect to the Freedericksz threshold (32). *TPDS* with azimuthal modulation (*MODE P5*) now involves a convective flow with the integral wavevector b_P. The aperiodic *MODE N5* is associated with azimuthal backflow and is favourable if the dimensionless growth rate $R_S < 1$. (a,b) Variations of R_S and b_P with R_X for R_{21} = (1) 1.02 (2) 1.035 (3) 1.12. (c,d) Plots of R_S and b_P versus R_{21} for R_X = (1) 4 (2) 6. The dependence of R_S on R_{21} is weak. The changeover from *TPDS* to the aperiodic mode occurs discontinuously with respect to b_P (section 4.2)

It is worth comparing (17) with the corresponding condition for the flat geometry. Consider the homeotropically aligned sample between two planes $z = \pm h$. Let the x and y axes also be fixed. Let ϕ and θ be the deformations in the xz and the yz planes, respectively. For homeotropic anchoring, there exists uniaxial symmetry about z axis. We expect that the anchoring strength for ϕ and θ is the same. In cylindrical geometry, this may not be true. Even though the alignment layer imparts a homeotropic alignment, the fact that this layer is curved about z axis may make the anchoring strength for ϕ (deformation in the $r - \psi$ plane) different from that for θ (distortion in the $r - z$ plane). For example, $A_{\phi 1}$ and $A_{\theta 1}$ of (18) may be different. We shall, however, study only rigid anchoring.

In calamitics such as 5*CB* (23), $\eta_C > \eta_A > \eta_B$ and the torque viscosity μ_2 is much stronger than μ_3. The application of **H** normal to the homeotropic $\mathbf{n_0}$ generally does not produce *TPDS* but only *AR* in flat samples. A reason for this [8] is that the low effective viscosity ($\approx \gamma_1 - \mu_2^2/\eta_C$) for *AR* cannot be further reduced if the perturbations have spatial periodicity. As the director in discotic nematics is normal to the planes of the disk-like molecules, the possibility was recognized [28] that the discotic phase may possess a strong μ_3 and a much weaker μ_2 so that the Miesowicz viscosities now satisfy the condition $\eta_B > \eta_A > \eta_C$ which is opposite to that valid for the calamitic phase. Molecular dynamic simulations [29] support this conjecture. In such a material the effective viscosity for *AR* is sufficiently high so that the appearance of *TPDS* in the homeotropic geometry becomes a distinct possibility. The application of a strong, destabilizing **H** along the homeotropic $\mathbf{n_0}$ in a discotic nematic with negative χ_A does show the occurrence of *TPDS* [30]. The results of [30] have been qualitatively substantiated [31] on the basis of the conjecture of [28]. For presenting numerical results in this section, the material parameters of (23) are adopted with the values of η_B and η_C interchanged:

$$(K_1\,,\ K_2\,,\ K_3\,) = (5.21\,,\ 2.71\,,\ 6.67)\,10^{-7}\ \text{dyne}\ ;$$
$$(\eta_A\,,\ \eta_B\,,\ \eta_C\,,\ \gamma_1\,,\ \nu_1) = (0.358\,,\ 0.973\,,\ 0.161\,,\ 0.728\,,\ 0.412)\ \text{poise}. \tag{39}$$

It is known [32] that some discotic nematics have $K_1 > K_3$. Such a material can be studied by a further interchange of K_1 and K_3 values in (39). As the nature of destabilizing fields is different for the two signs of χ_A, it is instructive to study both cases.

5.1 Discotic Nematic; $\chi_A > 0$

Consider first the axial field (4). The field does not affect ϕ but couples only to θ. With a dependence on r and ignoring dynamic effects, θ is a mixture of splay and

bend distortions. The Freedericksz field H_F can be numerically determined from (34) and the reduced field R_Z defined as in section 3.3. *AR* (**MODE N6**) is associated with θ and the back-flow v_z; *MODE N6* grows with a positive rate, s_A, if $R_Z > 1$. TPDS with periodicity along z (**MODE P6**) is associated with θ, v_r, v_z and p whose variation is similar to that given in section 3.4; hence, *MODE P6* is convective in nature. Solving (9), (34), (35) and (37) as in section 3.4, the maximum growth rate s_P as well as the dimensionless *PWV*, Q_Z, can be determined as functions of R_Z for different R_{21} (Figures 9a, 9b). The qualitative similarity with Figures 5a, 5b is striking. *MODE P6* grows faster than *MODE N6* when R_Z is high enough. When R_Z reaches a lower limit R_{ZC}, the growth rates of *MODE P6* and *MODE N6* become equal. Thus, *MODE N6* is more favourable when R_Z is sufficiently low. The crossover between *MODE P6* and *MODE N6* is discontinuous; Q_Z is non-zero at some Q_{ZC} when R_S becomes unity. When R_{21} is enhanced, *MODE N6* exists over a broader R_Z range (compare curves 1 and 2 in Figures 9a, 9b). Plots of R_{ZC} and Q_{ZC} as functions of R_{21} (not included here) are similar to those of Figures 5c, 5d.

On the other hand, the azimuthal field (5) couples to ϕ but not to θ. When Y exceeds the *NPD* threshold Y_F given by,

$$Y_F^2 = \frac{K_3}{\chi_A}\left(\left(\frac{\pi}{\ln(R_{21})}\right)^2 + 1 - \frac{K_1}{K_3}\right), \tag{40}$$

a splay – bend deformation ϕ sets in. The reduced field R_Y can be used to measure Y in terms of Y_F. *AR* (**MODE N7**) involves a coupling between ϕ and ω. The growth rate, s_A, of *MODE N7* is computed numerically from (33), (36). When $R_Y \to 1$, $s_A \to 0$. As the field is azimuthal, *TPDS* (**MODE P7**) should set in with azimuthal periodicity; ϕ and ω now couple with v_r and p showing that *MODE P7* is convective. The dependence of perturbations as well as the method of solution are as in section 4.2 except that ϕ replaces θ; the dimensionless *PWV*, b, is varied in steps of unity. The equations connecting the perturbations are (9), (33), (35) and (36). When R_Y is high enough, the growth rate of *MODE P7*, s_P, corresponds to *PWV*, b_P, taking a suitable integral value. Figures 9c, 9d show the dependence of R_S and b_P when the field strength is varied. The transition between *MODE P7* and *MODE N7* is found to be discontinuous at a given R_{21}; when $s_P$and s_A become equal, b_P does not vanish. A small increase in R_{21} causes a substantial change in the number of domains (b_P).

The results of this section remain qualitatively unchanged when K_1 and K_3 in (39) are interchanged. K_1 is associated with the z variation of *MODE P6* (equation 34) as well as the ψ variation of *MODE P7* (equation 33). Hence, an increase in K_1 has a deleterious effect on the formation of *TPDS*; ie., lower

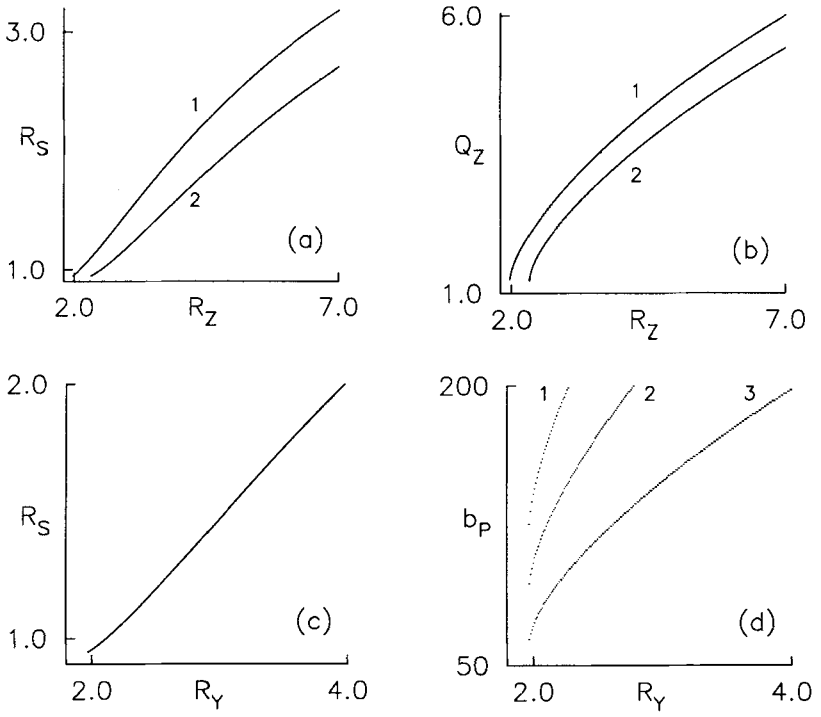

FIGURE 9 Nematic with radial initial alignment with parameters (39) typical of a discotic material. Boundaries impose rigid anchoring. Diamagnetic anisotropy, χ_A, is positive. R_S is the reduced growth rate of *TPDS* with respect to the corresponding aperiodic reorientation. (a,b) Effect of axial field (4). *TPDS* with periodicity along z (*MODE P6*) occurs if the reduced field, R_Z, is high; Q_Z is the dimensionless periodicity wavevector. Curves are drawn for R_{21} = (1) 1.02 (2) 6 (c,d) Effect of azimuthal field, (5). The reduced field, R_Y, is calculated in terms of the threshold (40). At high enough R_Y, *TPDS* with azimuthal modulation (*MODE P7*) can set in with the integral wavevector, b_P. Results correspond to R_{21} = (1) 1.02 (2) 1.027 (3) 1.04. In (c), the variation of R_S is practically identical for the three R_{21}; however. a small increase in R_{21} produces a significant diminution in the number of domains (section 5.1)

growth rate and wavevector at fixed R_{21} and R_H as well as an increased cut-off field below which only *AR* occurs.

5.2 Discotic Nematic; $\chi_A < 0$

This case is the analogue of the configuration studied in a flat sample [30]. The material parameters (39) are used with χ_A assuming a negative sign. The radial field (6) which is the only destabilizing influence couples with both ϕ and θ. In the most general case, *TPDS* should possess periodicity along z and ψ. The

assumption of periodicity along one symmetry direction simplifies the presentation. Such solutions in cylindrical geometry are similar to those that occur in the flat geometry (Appendix 4).

The *NPD* threshold is obtained by assuming that ϕ and θ have only r dependence. The two perturbations get decoupled with the threshold for θ, X_1, being given by

$$X_1^2 = \frac{K_3}{-\chi_A}\left(\left(\frac{\pi}{\ln(R_{21})}\right)^2 - \frac{K_1}{K_3}\right).$$

X_1 is lower than the threshold for ϕ, X_2, defined by

$$X_2^2 = \frac{K_3}{-\chi_A}\left(\left(\frac{\pi}{\ln(R_{21})}\right)^2 + 1 - \frac{K_1}{K_3}\right).$$

Hence, we employ X_1 to define the reduced field, R_X. The reason for X_2 being higher than X_1 is the additional elastic deformation energy associated with ϕ.

AR occurs in two independent forms; while ϕ couples with the back-flow ω, θ is modified by the flow v_z. At $R_X > 1$, the growth rate of the $\theta - v_z$ set (which we call **MODE N8**) is slightly higher than that of the $\phi - \omega$ set. Hence, the growth rate of *MODE N8*, s_A, can be employed for comparison with the growth rate of *TPDS*.

TPDS can occur with either axial or azimuthal periodicity. We first consider axial periodicity. When dependence is assumed on r, z and t, the perturbations split into two separate sets. **MODE P8** represents convective flow connecting the variables θ, v_r and v_z. We remember that *PWV*, **q**, now lies along z. Of the perturbations, θ is the component of **n** along z; similarly, v_r and v_z are the components of **V** in the rz plane that contains **q**. When R_X is high enough, *MODE P8* has a faster growth rate than *MODE N8*. With the parameters (39), the curves of R_S and Q_Z as functions of R_X are similar to those found in Figures 9a, 9b; in particular, Q_Z varies continuously with R_X. *MODE P8* gets discontinuously quenched when R_X becomes sufficiently small. The remaining perturbations, ϕ and ω form an independent set. Clearly, these are components of **n** and **V** along ψ, ie., normal to the rz plane. In spite of the coupling between ϕ and **H**, these variables do not grow even when the **H** imposed is strong (say, $R_X = 8$). The analogy with the flat sample configuration (Appendix 4) is clear.

When periodicity is assumed along ψ, the perturbations get regrouped. Clearly, θ and v_z are the z components of **n** and **V**, respectively. These perturbations cannot grow even at reasonably high R_X as they are normal to *PWV* which now lies along the azimuthal direction (see Appendix 4). **MODE P9** is associated with the remaining variables, ϕ, ω and v_r; while ϕ is the ψ component of **n**, ω and v_r are

components of **V** lying in the $r\psi$ plane. MODE *P9* represents a convective flow in the $r\psi$ plane except that *PWV* is now discrete. At sufficiently high R_x, *MODE P9* grows faster than *MODE N8*; the plots of R_S and *PWV* are similar to those found in Figures 9c, 9d if the parameters (39) are employed.

Thus, when a radial **H** is imposed, *TPDS* can be either *MODE P8* or *MODE P9*. Both modes involve convective flow. The question is, whether the two modes of *TPDS* have the same growth rate. When R_{21} is close to unity and R_X sufficiently high, the two modes are found to have practically the same growth rate. On the other hand, when R_{21} is high and R_X sufficiently low, *MODE P8* grows slightly faster than *MODE P9*. Within the framework of the assumptions made, it can be stated that *TPDS* in a discotic nematic with negative χ_A tends to have axial periodicity when the imposed radial **H** is not strong; under a strong **H**, however, *TPDS* may have both axial and azimuthal modulations.

6. CONCLUSIONS

A nematic with moderate elastic anisotropy is confined to the annular space between two coaxial cylinders with the director, $\mathbf{n_0}$, initially aligned along one of the symmetry directions. The lengths of the cylinders is assumed to be large compared to the sample thickness (difference in the radii). If a gradually strengthening **H** is imposed parallel to (or normal to) $\mathbf{n_0}$, a static aperiodic deformation occurs above a Freedericksz threshold [15–17] provided that χ_A is negative (or positive). Using this threshold, a reduced field strength is defined. If **H** with reduced strength exceeding unity is suddenly impressed on $\mathbf{n_0}$, the director field undergoes reorientation and the director distortion becomes time dependent; in some cases, transient flow is also induced and couples with the director field. When the reduced strength is moderately large, the reorientation is aperiodic (*AR*) with an instantaneous growth rate, s_A, which can be calculated as indicated in earlier work [8–10, 17].

When the imposed **H** is stronger than a threshold, the reorientation is periodic (*TPDS*) with an instantaneous growth rate, s_P, associated with a periodicity wavevector (*PWV*) whose magnitude and direction depend strongly on the configuration studied. In sections 3 to 5, the attributes of *TPDS* in different configurations of cylindrical geometry are compared. For simplicity, *PWV* is assumed to be either axial or azimuthal in a given case. Then, $R_S = s_P/s_A$ is the reduced growth rate. If $R_S > 1$, we say that *TPDS* is more favourable than *AR*. If the material parameters are those of a calamitic nematic *TPDS* should occur when n_0 is axial or azimuthal (sections 3 and 4). With (hypothetical) parameters corresponding to a typical discotic nematic, *TPDS* should set in when $\mathbf{n_0}$ is radial (section

5). The results of this work reduce to the corresponding results for flat plates when the radii ratio, R_{21} is close to unity (Appendices 3 and 4). By using R_S and the dimensionless *PWV*, results can be expressed in terms of R_{21} and the reduced field when the director anchoring is rigid. A further quantity, Σ, can be employed when the director anchoring energy is finite (section 3.2).

A weakening of **H** causes the *PWV* of *TPDS* to diminish. For axial modulation, the *PWV* diminishes continuously with the reduced field (sections 3, 5.1). When the modulation is azimuthal, the *PWV* takes integral values (sections 4, 5.2); then *PWV* represents half the number of domains associated with *TPDS*. Hence, the change of *PWV* with reduced field is discontinuous when *TPDS* has azimuthal periodicity. The nature of the quenching of *TPDS* at threshold depends on the configuration studied. When *TPDS* involves a combination of twist and bend and the velocity is non-convective (does not possess a component directed against the cylinder walls), *AR* is associated with a twist distortion that does not couple with flow; in such a case, the *PWV* diminishes to zero with the reduced field and the transition from *TPDS* to *AR* is continuous (sections 3.1–3.3, 4.1). On the other hand, periodic splay and bend distortions couple with a convective flow component as well as the pressure perturbation in *TPDS;* then, *AR* contains a splay – bend deformation that occurs with non-periodic backflow (sections 3.4, 3.5, 4.2, 5). In such cases, *PWV* remains non-zero when the the growth rates of *TPDS* and *AR* become equal; hence, the quenching of *TPDS* is discontinuous. The dimensionless threshold below which *AR* is more favourable is independent of R_{21} when **H** is constant in the sample (section 3.3); this threshold varies with R_{21} (sections 3.1, 3.2, 3.4) when **H** depends on r. Some limitations of the present work must be borne in mind.

The anchoring strength (section 3.2) is different for different surface treatments and cannot be varied continuously in real experiments; a similar statement can be made for the ratio of the cylinder radii. The length of the cylinders is assumed to be large compared to the difference in the radii and *PWV* for z modulation is assumed to vary continuously with different control parameters. In an experiment the cylinders have finite length. Boundary conditions have to be imposed on **n** and **V** at the end planes that limit the sample. Hence, the number of domains for z periodicity as well as *PWV* must change discontinuously with R_{21} or the reduced field.

Results for the radial **H** (sections 3.4, 3.5, 4.2, 5.2) have been included for completeness. It would have been more realistic to replace **H** by an electric field, **E.** This has not been attempted here for reasons given in [20]. Qualitative arguments show [33] that when a nematic with high dielectric anisotropy is confined between coaxial cylinders, the action of **E** may result in static periodic distortions. A complete discussion will also have to include the effects of electrical

conductivity which may cause convective instabilities [1–4]. Hence, the effects of **E** will be studied separately.

The expression for the body force density due to **H** (Appendix 1) is approximate. It leads to some simplification as the elastic and magnetic terms can be removed from the balance equations for linear momentum. A more correct approach assumes that **H** is perturbed by **H′** which is derivable from a scalar potential. The vanishing of the divergence of the total magnetic field then connects the gradients of **H′** to those of the director perturbations in a separate equation. Terms containing **H′** should occur in the magnetic torque as well as the magnetic body force. Appropriate boundary conditions should also be imposed on **H′**. This approach will be attempted in future.

Two related aspects can be stated together. (1) The non-stochastic continuum theory has been employed here to calculate the instantaneous growth rate and *PWV* of *TPDS* in the linear perturbation limit. In a real experiment, both the growth rate and *PWV* are functions of time. It has been shown [34] that by including thermal noise in the governing equations a more complete picture of *TPDS* can be obtained. (2) Soon after *TPDS* sets in, both the director and velocity fields become non-linear; after the elapse of sufficient time, the system reaches its final equilibrium state. The small perturbations approximation cannot be used to predict the nature of *TPDS* well after the instant at which **H** is impressed.

Finally, it is worth commenting on the equilibrium pressure, p_o (Appendix 1) which becomes a function of r even though the effect of gravity is absent. This nature of p_o arises from gradients in the equilibrium director configuration and **H**. In an isotropic liquid, p_o should be constant at equilibrium when the effect of gravity is excluded. The question is, how to understand the fact that p_o is a function of r in a nematic; how can the fluid sustain such a pressure in a state of equilibrium ? Two viewpoints present themselves.

i. An isotropic liquid has only the translational degree of freedom. But a nematic has the additional, rotational degree of freedom, viz., the director orientation. If the equilibrium orientation is globally distorted (as in (2) and (3)), the equilibrium part of the stress is a function of r. Then, the stress gradients can only be balanced to ensure equilibrium if p_o is also dependent on r.

ii. We use governing equations [1–4] that are derived for a three dimensional mass of fluid in which the velocity and director fields are functions of all three space coordinates. For simplicity, we employ a mathematical model in which the fields are functions of only two coordinates. In the process, we solve the equations for an (artificial) two dimensional sample. Suppose the fields are independent of z. Then the problem is solved in the $r\psi$ plane. The location of this plane in the sample is arbitrary. It is tacitly assumed that whatever happens in one $r\psi$ plane happens in all others; but there is nothing

in the mathematics employed which explicitly establishes this. The dependence of p_o on r is a consequence of the unphysical mathematical model.

References

[1] P. G. de Gennes and J. Prost, *The Physics of Liquid Crystals*, (Clarendon Press, Oxford. 1993).

[2] S. Chandrasekhar, *Liquid Crystals*, (Cambridge University Press, 1992).

[3] L. M. Blinov and V.G. Chigrinov, *Electrooptic Effects in Liquid Crystal Materials*, (Springer Verlag, 1993).

[4] S. A. Pikin, *Structural Transformations in Liquid Crystals*, (Gordon and Breach, 1991).

[5] H. J. Deuling, *Solid State Physics Supplement*, **14,** 77 (1978); this is a review on *NPD* caused by **B** and **E**.

[6] C. Gooden, R. Mahmood, A. Brisbin, A. Baldwin, D.L. Johnson and M.E. Neubert, *Phys. Rev. Lett.*, **54,** 1035 (1985); F. Lonberg and R. B. Meyer, *ibid* **55,** 718 (1985).

[7] J. Cognard, *Mol. Cryst. Liquid Cryst. Suppl.*, **1,** 1 (1982) and B. Jerome, *Rep. Progr. Phys.*, **54,** 391 (1991) are reviews on interfacial properties of nematics.

[8] P. Pieranski, F. Brochard and E. Guyon, *J. Phys. France*, **34,** 35 (1973).

[9] E. F. Carr, *Mol. Cryst. Liquid Cryst.*, **34** (Letters). 159 (1977); for reviews see G. Srajer, S. Fraden and R. B. Meyer, *Phys. Rev. A*, **39,** 4828 (1989); U. D. Kini, *J. Phys. II*, **1,** 225 (1991).

[10] E. Guyon, R. B. Meyer and J. Salan, *Molec. Cryst. Liquid Cryst.*, **54,** 261 (1979).

[11] S. Ciaponi and S. Faetti, *Liq. Cryst.*, **8,** 473 (1990).

[12] P. E. Cladis, in *Nematics. Mathematical and Physical Aspects*, Edited by J.-M. Coron, J.-M. Ghidaglia and F. Helein, (Kluwer Academic Publishers, London), 1991, p65; see also references therein.

[13] E. Dubois-Violette and P. Manneville, *J. Fluid Mech.*, **89,** 273 (1978).

[14] C. R. Carrigan and E. Guyon, *J. Phys. France Letters*, **36,** 145 (1975).

[15] F. M. Leslie, *J. Phys. D*, **3,** 889 (1970); R. J. Atkin and P. J. Barratt, *Q. J. Mech. Appl. Math.*, **26,** 109 (1973).

[16] U. D. Kini, *J. Phys. France*, **49,** 527 (1988).

[17] P. Palffy-Muhoray, A. Sparavigna and A. Strigazzi, *Liq. Cryst.*, **14,** 1143 (1993); P. J. Barrat and B. R. Duffy, *Liquid Cryst.*, **19**, 57 (1995); ibid *J. Phys. D*, **29,** 1551 (1996).

[18] J. Chen, D.L. Johnson, P.J. Bos, S. Sprunt, J. Lando and J.A. Mann Jr., *Appl. Phys. Lett.*, **68,** 885 (1996).

[19] L. D. Landau and I. M. Lifshitz, *Electrodynamics of Continuous Media*, (Pergamon Press, 1984).

[20] While the axial or azimuthal **B** is experimentally feasible, the radial field is not. When the sample is flat, the axial or the azimuthal **B** becomes a field in the sample plane; the radial **B** is the only component normal to the sample walls. In contrast, it seems feasible to generate a radial or an axial **E** but not the azimuthal one. A radial **E** would arise by the application of a potential difference between suitably treated cylindrical surfaces. This would have been a good substitute for the radial **B.** However, **E** gets modified by director perturbations which makes it necessary to include Maxwell's equations explicitly into the solution so that the modifications of **E** are connected to the director gradients.

[21] η_A corresponds to the viscosity with $\mathbf{n_0}$ being normal to the plane of shear. When $\mathbf{n_0}$ is in the shear plane but along (or normal) the flow direction, the viscosity is η_B (or η_C). In terms of the viscosities μ_k (see ref. 2), $\gamma_1 = \mu_3 - \mu_2$; $\eta_A = \mu_4/2$; $\eta_B = (\mu_3 + \mu_4 + \mu_6)/2$; $\eta_C = (\mu_5 + \mu_4 - \mu_2)/2$. The Parodi relation [2] requires that $\mu_6 = \mu_2 + \mu_3 + \mu_5$. The torque viscosities can be written as $\mu_2 = (\eta_B - \eta_C - \gamma_1)/2$; $\mu_3 = (\eta_B - \eta_C + \gamma_1)/2$.

[22] A. J. Hurd. S. Fraden, F. Lonberg and R. B. Meyer, *J. Phys. France*, **46**, 905 (1985); the extensional viscosity can be expressed in terms of the μ_k as $\nu_1 = (\mu_1 + \mu_4 + \mu_5 + \mu_6)/2$.

[23] G. P. Crawford, R. J. Ondris-Crawford, J.W. Doane and S. Zumer, *Phys. Rev. E*, **53**, 3647 (1996) and references therein. According to the expression of the deformation free energy density in this work, $0 \leq K_{24} \leq 2\ K_1$or $0 \leq K_{24} \leq 2\ K_2$, whichever is less. For a calamitic nematic, the latter condition is employed to determine the maximum value of K_{24}.

[24] U. D. Kini, *J. Physique*, **47,** 693 (1986).

[25] L. A. Pipes and S. A. Hovanessian, *Matrix Computer Methods in Engineering*, (John Wiley, 1969).
[26] The elastic constant values are from J.D. Bunning, T.E. Faber and P.L. Sherrell, *J. Phys. France*, **42,** 1175 (1981). The viscosities are from G.P. Chen, H. Takezoe and A. Fukuda. *Liq. Cryst.*, **5**, 341 (1989) and correspond to $\mu_1 = 0$ (assumed), $(\mu_2, \mu_3, \mu_4, \mu_5) = (-0.77, -0.042, 0.716, 0.46)$ poise; by the Parodi relation, $\mu_6 = -0.352$ poise.
[27] F. Lonberg, S. Fraden, A.J. Hurd and R. B. Meyer, *Phys. Rev. Lett.*, **52,** 1903 (1984).
[28] G. E. Volovik, *JETP Letters*, **31**, 273 (1980).
[29] H. Sollich, D. Baalss and S. Hess, *Molec. Cryst. Liquid Cryst.*, **168,** 189 (1989).
[30] M. R. Kuzma, *Phys. Rev. Lett.*, **57,** 349 (1986).
[31] S. Fraden and R. B. Meyer, *Phys. Rev. Lett.*, **57,** 3122 (1986).
[32] T. Warmerdam, D. Frenkel and R. J. J. Zijlstra, *J. Physique*, **48**, 319 (1987).
[33] For references to earlier work, see U. D. Kini, *Liquid Cryst.*, **24**, 177 (1998).
[34] F. Sagues and M. San Miguel, *Phys. Rev. A*, **32**, 1843 (1985).

Appendix 1

Let $(r, \psi, z) = (x_1, x_2, x_3)$ be the cylindrical coordinates. Let n_i be the physical components of the director field along the x_i axis and $n_{i,k}$ the physical componenets of the director gradient; the subscriped comma in $n_{i,k}$ denotes covariant differentiation of n_i with respect to the coordinate x_k. Then, the body force density corresponding to curvature elasticity is [1, 2]

$$f_k = -\left(\Pi_{j,m} n_{m,k}\right), j \; ; \quad \Pi_{jm} = \frac{\partial W}{\partial n_{m,j}}$$

where W is the Oseen – Frank elastic energy density; repeated indices are summed over. The body force density due to the magnetic field is

$$g_k = M_{jk,j} \; ; \quad M_{jk} = \frac{B_j H_k}{4\pi}$$

where M_{jk} is the Maxwell stress; $B_k = H_k + 4\pi\chi_{kj} H_j$; $\chi_{kj} = \chi_\perp \delta_{kj} + \chi_A n_k n_j$; $\chi_\perp$ is the diamagnetic susceptibility normal to the director. In the present picture where we ignore perturbations in **H** caused by director gradients, we assume that **B** is divergenceless (ie., that $B_{m,m} = 0$) and write

$$g_k = \frac{B_j H_{k,j}}{4\pi}.$$

Then, the total body force density becomes

$$F_m = f_m + g_m.$$

In general, $\mathbf{F} = \mathbf{F^0} + \mathbf{F'}$ where $\mathbf{F^0}$ is independent of director perturbations and $\mathbf{F'}$ depends on them. At equilibrium, we require that

$$\mathbf{F^0} = \nabla p_o$$

where p_o is the equilibrium hydrostatic pressure. When $\mathbf{n_0}$ is axial (section 3), the only non-zero component of **F** to first order in small quantities is

$$F_1^0 = -\frac{X^2}{4\pi r^3}\left(1 + 4\pi\chi_\perp\right)$$

when **H** is radial; this is also true for azimuthal **H** except that X is replaced by Y. As $\mathbf{F'} = \mathbf{0}$, the body force terms due to elasticity and magnetic field are absent in (12) – (14) which govern the perturbations.

When $\mathbf{n_0}$ is azimuthal, $\mathbf{F'}$ has non-zero components which now appear in (28) - (30). The perturbation-independent part is defined by

$$F_1^0 = \frac{K_3}{r^3} - \frac{X^2}{4\pi r^3}\left(1 + 4\pi\chi_\perp\right) \quad \text{or} \quad F_1^0 = \frac{K_3}{r^3} - \frac{Y^2}{4\pi r^3}\left(1 + 4\pi\chi_{||}\right)$$

when **H** is radial or azimuthal; $\chi_{||}$ is the diamagnetic susceptibility along the director. If **H** is oblique with both radial and axial components,

$$F_1^0 = \frac{K_3}{r^3} - \frac{X^2}{4\pi r^3}(1 + 4\pi\chi_\perp);$$

the axial component contributes the term proportional to m_5 only to the perturbation part (29).

Suppose $\mathbf{n_0}$ is radial. Then the only non-zero component of the perturbation independent part is

$$F_1^0 = \frac{K_1}{r^3} - \frac{X^2}{4\pi r^3}(1 + 4\pi\chi_{||}) \quad \text{or} \quad F_1^0 = \frac{K_1}{r^3} - \frac{Y^2}{4\pi r^3}(1 + 4\pi\chi_\perp)$$

depending upon whether **H** is radial or azimuthal. The perturbation dependent part is included in (36).

Appendix 2

A brief outline of the numerical technique is presented (see Appendix of [24]) by using *MODE N*1 and *MODE P*1 as examples. The material parameters are fixed. Convenient values are assigned to h and R_{21} from which the radii of the cylinders can be calculated. The reduced field is sufficiently strong to ensure positive growth rates of both instability modes. Rigid anchoring (20) is assumed but the results can be easily extended to the case of weak anchoring (section 3.2).

The *ODE* related to *MODE* N1 is found from (11),

$$(\xi + a)^2 \frac{d^2P}{d\xi^2} + (\xi + a)\frac{dP}{d\xi} + P\left[R_Y^2 + \left(\frac{\pi R_Y}{\ln(R_{21})}\right)^2 - 1\right] - \left(\frac{\gamma_1 sh^2}{K_2}\right)(\xi + a)^2 P = 0, \tag{A1}$$

and is to be solved with the boundary conditions,

$$P = 0 \quad at \quad \xi = \pm 1. \tag{A2}$$

The function P is expanded in non-negative powers of ξ in the form

$$P = \sum_{k=0}^{C} \Phi_k \xi^k \tag{A3}$$

where Φ_k are constants and C an integer for which a high enough value is chosen as described below. By substituting (A3) in (A1) and by comparing powers of ξ, every Φ_k can be expressed in terms of the two leading coefficients, Φ_0 and Φ_1, such that

$$\begin{aligned} \Phi_k &= \alpha_k \Phi_0 + \beta_k \Phi_1, \quad k = 0, \ldots, C; \\ \alpha_0 &= 1; \quad \beta_0 = 0; \quad \alpha_1 = 0; \quad \beta_1 = 1. \end{aligned} \tag{A4}$$

For $1 < k \leq C$, the α_k and β_k can be computed recursively for given values of other parameters. The boundary conditions (A2) reduce to.

$$\begin{aligned} &\Phi_0 \Delta_{11} + \Phi_1 \Delta_{12} = 0; \quad \Phi_0 \Delta_{21} + \Phi_1 \Delta_{22} = 0; \\ &\Delta_{11} = 1 + \sum_{k=2}^{C} \alpha_k; \quad \Delta_{12} = 1 + \sum_{k=2}^{C} \beta_k; \\ &\Delta_{21} = 1 + \sum_{k=2}^{C} \alpha_k (-1)^k; \quad \Delta_{22} = -1 + \sum_{k=2}^{C} \beta_k (-1)^k. \end{aligned} \tag{A5}$$

The Δ_{ij}, $i, j = 1,2$ are the components of the second order matrix D_2. Clearly, Φ_0 and Φ_1 will exist only if D_2 has a vanishing determinanat:

$$\det(\mathcal{D}_2) = 0. \tag{A6}$$

By varying s with other parameters fixed, (A6) is found to be satisfied only at select values of s. In this sense, the solution of (A1) and (A2) reduces to the solution of an eigenvalue problem. Each value of s satisfying (A6) can be regarded as an eigenvalue of D_2. Corresponding to each eigenvalue, only the ratio of Φ_0 and Φ_1 can be found; the absolute values of Φ_0 and Φ_1 are never known. Hence, Φ_0 and Φ_1 can be regarded as the components of the eigenvector of D_2 belonging to the particular eigenvalue.

At the given R_Y, the highest positive $s = s_A$ satisfying (A6) is found by iteration. This is conveniently achieved by finding the least positive relaxation time (= $1/s$) at which (A6) is satisfied. It is clear from (A1) that $s_A h^2$ is a function of R_Y and R_{21}:

$$s_A h^2 = S_1 (R_Y, R_{21}). \tag{A7}$$

The solution for *MODE P*1 is similar to that for *MODE N*1. Equations (11) and (13) take the form

$$\begin{aligned}
&(\xi + a)^2 \frac{d^2 P}{d\xi^2} + (\xi + a) \frac{dP}{d\xi} + P \left[R_Y^2 + \left(\frac{\pi R_Y}{\ln (R_{21})} \right)^2 - 1 \right] \\
&\quad - \left(\frac{\gamma_1 s h^2}{K_2} + \frac{K_3}{K_2} Q^2 \right) (\xi + a)^2 P - \frac{\mu_2 Q}{K_2} (\xi + a)^3 \Omega' = 0 \\
&(\xi + a) \frac{d^2 \Omega'}{d\xi^2} + 3 \frac{d\Omega'}{d\xi} - \left(\frac{\eta_C}{\eta_A} Q^2 + \frac{\rho s h^2}{\eta_A} \right) (\xi + a) \Omega' \\
&\quad - \frac{\mu_2 Q s h^2}{\eta_A} P = 0 \\
&Q = q h; \quad \Omega' = \Omega h^2
\end{aligned} \tag{A8}$$

where Q is a dimensionless wavevector. Expressing the functions $P$and Ω' in the form,

$$P = \sum_{k=0}^{C} \Phi_k \xi^k; \quad \Omega' = \sum_{k=0}^{C} \Omega_k \xi^k, \tag{A9}$$

substituting in (A8) and comparing powers of ξ, it is found that Φ_0, Φ_1, Ω_0 and Ω_1 can be used as a basis to express all other coefficients Φ_k and Ω_k. The boundary conditions

$$P = 0, \quad \Omega' = 0 \quad \text{at} \quad \xi = \pm 1 \tag{A10}$$

reduce to four homogeneous simultaneous equations whose compatibility requires that the corresponding fourth order determinant vanish:

$$\det(\mathcal{D}_4) = 0. \tag{A11}$$

Chio's method (see [25]) is convenient for the calculation of det(D) when the dimension of D is 4 or higher. Using (A11), the highest growth rate, $s = s_f$ can be determined. Fixing all parameters and varying only Q, $s_f(Q)$ can be studied as a function of Q. Clearly, $s_f \to s_A$ when $Q \to 0$. When Q increases from zero, s_f also increases and attains the maximum, s_P, when $Q = Q_Z$ corresponding to $q = q_P$:

$$s_P = s_f\,(Q_Z)\,.$$

We regard s_P as the *instantaneous growth rate* for *MODE P*1 and q_P as *PWV* at the time of applying **H;** Q_Z is the corresponding dimensionless wavevector associated with *MODE P*1. From (A8), the following relationships can be written down:

$$s_P h^2 = S_2\,(R_Y, R_{21})\;;\quad Q_z = S_3\,(R_Y, R_{21})\,.$$

The reduced growth rate of *MODE P*1 relative to that of *MODE N*1, R_S, can be defined as,

$$R_S = \frac{s_P}{s_A}.$$

This enables a study of R_S and Q_Z as functions of R_Y and R_{21}.

The computation was performed with double precision arithmetic on a Dec Alpha Workstation at the Raman Research Institute. The calculated quantities such as R_S and Q_Z agree to better than four decimal places at $C = 30$ and $C = 50$. For uniformity, the integer C is fixed at 70 for all calculations. This is found to be adequate for the range of R_{21} and reduced fields employed in this work. Using different sets of R_1, R_2 values corresponding to the same R_{21} but different h, one can check through computation that R_S and Q_Z are independent of h. The definitions of dimensionless wavevector and growth rate are similarly given in all the remaining cases. The scaling relations for the different cases can also be written down by an inspection of the relevant governing equations.

Appendix 3

The results of [11] are recapitulated for comparison. Consider the nematic aligned along x between plates $z = \pm h$ subjected to the action of $\mathbf{H} = (0, H_y, 0)$ along y. The twist anchoring strength is A_ϕ at both plates and Σ (24) is the relevant dimensionless parameter. The periodically perturbed director

$$\mathbf{n} = (1, \phi(z)\cos(q_x x)\exp(st), 0)$$

and velocity

$$\mathbf{V} = (0, v_y(z)\sin(q_x x)\exp(st), 0)$$

fields get coupled so that the governing equations

$$\frac{d^2\phi}{d\xi^2} + U_1\phi + U_2 v_y = 0; \quad U_3\phi + \frac{d^2 v_y}{d\xi^2} + U_4 v_y = 0; \xi = \frac{z}{h};$$
$$U_1 = \frac{\chi_A H_y^2 h^2 - K_3 Q_x^2 - \gamma_1 s h^2}{K_2}; \quad U_2 = -\frac{h\mu_2}{K_2}Q_x;$$
$$U_3 = -\frac{h\mu_2 s}{\eta_A}Q_x; \quad U_4 = -\frac{\eta_C}{\eta_A}Q_x^2; \quad Q_x = h q_x \qquad (A12)$$

are to be solved with the boundary conditions

$$\frac{d\phi}{d\xi} \pm \Sigma\phi = 0 \quad \text{and} \quad v_y = 0 \quad \text{at} \quad \xi = \pm 1. \qquad (A13)$$

Comparing (A13) with (18) we see that the boundary conditions for a flat sample do not depend on K_{24} in an analogous situation.

Following [11], the *NPD* threshold H_F is determined and the reduced field $R_H = H_y/H_F$ defined. At sufficiently high R_H, the growth rate of *AR*, s_A, can be calculated. For *TPDS* defined by (A12) – (A13). the growth rate, s_P, is the maximum $s_P = s(Q_P)$ occurring at the dimensionless *PWV*, $Q_x = Q_P$. Plots of Q_P and the dimensionless growth rate $R_P = s_P/s_A$ can be obtained as functions of R_H and Σ. These are found to be very close to the plots of R_S and Q_Z of Figures 3a, 3b when the ratio of the cylinder radii is close to unity. It can be shown that *TPDS* grows faster than *AR* only if

$$R_H > R_{HC}; \quad R_{HC}^2 = 1 + \frac{\eta_A\gamma_1 K_3}{\mu_2^2 K_2}\left[\frac{\Sigma^2 + \zeta + \Sigma}{\Sigma^2 + \zeta - \Sigma}\right]. \qquad (A14)$$

R_{HC} of (A14) gives an accurate representation of R_{YC} (Figures 3a, 3b) at which *MODE P*1 gets extinguished. One can recast (A14) to obtain $\Sigma = \Sigma_L$ for a given R_H such that for $\Sigma < \Sigma_L$, *TPDS* cannot exist. The plot of R_H versus Σ_L agrees very well with the critical boundary of Figure 2e drawn for $R_{21} = 1.02$. Σ_L

so calculated compare well with those appearing in Figures 3c, 3d. When the anchoring is rigid, $\Sigma \gg 1$ and

$$R_{HC} \to \left[1 + \frac{\eta_A \gamma_1 K_3}{\mu_2^2 K_2}\right]^{\frac{1}{2}} \qquad (A15)$$

which takes the value 1.443 for the parameters (23). Equation (A15) is the well known limiting field derived in earlier work [9, 27]. It must be remembered that the above solution considers the uncoupled mode having perturbations that are symmeteric with respect to $z = 0$. The other mode with antisymmetric perturbations grows more slowly and is not studied.

Appendix 4

The rectangular cartesian coordinate system is chosen such that the z axis is normal to the plates $z = \pm h$ between which the nematic with negative χ_A is homeotropically aligned. The equilibrium hydrostatic pressure is a constant. The inertial term containing ρ is ignored for convenience. For **H** applied along z, a convenient reduced field is

$$R_H = \frac{H}{H_3}; \quad H_3 = \frac{\pi}{2h}\left(\frac{K_3}{-\chi_A}\right)^{\frac{1}{2}}$$

where H_3 is the bend Freedericksz threshold. A strong **H** impressed along z can cause *AR* or *TPDS*. In the linear limit *AR* is represented by

$$\mathbf{n} = (\theta, \phi, 1); \quad \mathbf{V} = (v_x, v_y, 0)$$

where the perturbations are functions of z and t but split into two uncoupled sets, θ, v_x and ϕ, v_y, respectively. For $R_H > 1$, each set has the same, positive, growth rate, s_A, that can be computed from [8].

$$\zeta^3 + \frac{\mu_2^2 h^2 s_A}{\eta_C K_3}[\zeta - \tan(\zeta)] = 0$$

$$\zeta^2 = R_H^2 \frac{\pi^2}{4} - \frac{s_A h^2}{K_3}\left(\gamma_1 - \frac{\mu_2^2}{\eta_C}\right).$$

For periodic reorientation, the linearly perturbed director and velocity fields

$$\mathbf{n} = (\theta \sin(q_x x + q_y y)\exp(st), \quad \phi \sin(q_x x + q_y y)\exp(st), \quad 1)$$

$$\mathbf{V} = (v_x \sin(q_x x + q_y y), \quad v_y \sin(q_x x + q_y y), \quad v_z \cos(q_x x + q_y y))\exp(st)$$

are associated with the pressure perturbation, $p\cos(q_x x + q_y y)\exp(st)$; θ, ϕ, v_x, v_y, v_z and p are perturbations and functions of z. A derivation shows that the governing equations connect all the six perturbations. The *PWV*, **q**, breaks the cylindrical symmetry about z. It is instructive to resolve **n** and **V** into components along and normal to the plane containing the z axis and **q** so that

$$\theta_1 = q_x\theta + q_y\phi; \ \phi_1 = -q_y\theta + q_x\phi; \ v_1 = q_x v_x + q_y v_y; \ v_2 = -q_y v_x + q_x v_y;$$

v_z remains unchanged. The equation of continuity then takes the form

$$v_1 + \frac{dv_z}{d\xi} = 0; \quad \xi = \frac{z}{h},$$

with v_2 getting decoupled from v_1 and v_z. The governing equations also split into two uncoupled sets in which set 1,

$$\frac{d^2\theta_1}{d\xi^2} + \theta_1 \left[\left(\frac{\pi R_H}{2} \right)^2 - \left(\frac{\gamma_1 h^2}{K_3} \right) s - \left(\frac{K_1}{K_3} \right) Q^2 \right] - \left(\frac{\mu_2 h}{K_3} \right) \frac{dv_1}{d\xi} + \left(\frac{\mu_2 h}{K_3} \right) Q^2 v_z = 0$$

$$\frac{d^2 v_1}{d\xi^2} - \left(\frac{2\eta_A}{\eta_C} \right) Q^2 v_1 - \frac{\eta_D}{\eta_C} Q^2 \frac{dv_z}{d\xi} + \left(\frac{\mu_2 h}{\eta_C} \right) s \frac{d\theta_1}{d\xi} = - \left(\frac{h}{\eta_C} \right) Q^2 p$$

$$\frac{d^2 v_z}{d\xi^2} - \left(\frac{\eta_B}{2\nu_1} \right) Q^2 v_z + \left(\frac{\eta_D}{2\nu_1} \right) \frac{dv_1}{d\xi} + \left(\frac{\mu_3 h}{2\nu_1} \right) s \theta_1 = \left(\frac{h}{2\nu_1} \right) \frac{dp}{d\xi}$$

connects υ_1, υ_z and θ_1 and set 2,

$$\frac{d^2\phi_1}{d\xi^2} + \phi_1 \left[\left(\frac{\pi R_H}{2} \right)^2 - \left(\frac{\gamma_1 h^2}{K_3} \right) s - \left(\frac{K_2}{K_3} \right) Q^2 \right] - \left(\frac{\mu_2 h}{K_3} \right) \frac{dv_2}{d\xi} = 0$$

$$\frac{d^2 v_2}{d\xi^2} - \left(\frac{\eta_A}{\eta_C} \right) Q^2 v_2 + \left(\frac{\mu_2 h}{\eta_C} \right) s \frac{d\phi_1}{d\xi} = 0$$

relates ϕ_1 to υ_2; in the above, $Q^2 = h^2 (q_x^2 + q_y^2)$ is the square of a dimensionless *PWV*. All perturbations vanish at the boundaries. The material parameters (39) are employed. At sufficiently high R_H, the growth rate for set 1 shows a maximum $s_P = s(Q_P)$ at $Q = Q_p$ and $R_S > 1$. The plots of R_S and Q_P are very close to curves 1 in Figures 9a, 9b corresponding to $R_{21} = 1.02$. Even with a strong field (say, $R_H = 8$), the perturbations of set 2 do not exhibit growth. Thus, only the perturbations parallel to *PWV* exhibit *TPDS* while those normal to **q** damp out (see section 5.2)